ASYMMETRICAL NON-UNIFORM HEAT FLUX DISTRIBUTIONS FOR LAMINAR FLOW HEAT TRANSFER WITH MIXED CONVECTION IN A HORIZONTAL CIRCULAR TUBE

Izuchukwu F. Okafor, Jaco Dirker* and Josua P. Meyer**

Department of Mechanical and Aeronautical Engineering, University of Pretoria, Pretoria, Private Bag X20, Hatfield 0028, South Africa.

**Corresponding Author:*

Email Address: jaco.dirker@up.ac.za

Phone: +27 (0)12 420 2465

***Alternative Corresponding Author:*

Email Address: josua.meyer@up.ac.za

Phone +27 (0)12 420 3104

ABSTRACT

Non-symmetric heat flux distributions in terms of gravity in solar collector tubes influence buoyancy-driven secondary flow which has an impact on the associated heat transfer and pressure drop performance. In this study influence of the asymmetry angle (0°, 20°, 30° and 40°) with regard to gravity for non-uniform heat flux boundaries in a horizontal circular tube was investigated numerically. A stainless steel tube with an inner diameter of 62.68 mm, a wall thickness of 5.16 mm, and a length of 10 m was considered for water inlet temperatures ranging from 290 K to 360 K and inlet Reynolds numbers ranging from 130 to 2000. Conjugate heat transfer was modelled for different sinusoidal type outer surface heat flux distributions with a base-level incident heat flux intensity of 7.1 kW/m^2. It was found that average internal heat transfer coefficients increased with the circumferential span of the heat flux distribution. Average internal and axial local heat transfer coefficients and overall friction factors were at their highest for symmetrical heat flux cases (gravity at 0º) and lower for asymmetric cases. The internal heat transfer coefficients also increased with the inlet fluid

temperature and decreased with an increase in the external heat loss transfer coefficient. Friction factors decreased with an increase in fluid inlet temperature or an increase in the external heat loss transfer coefficients of the tube model.

Keywords: asymmetrical non-uniform heat flux boundary, secondary flow, heat transfer coefficients, friction factor

INTRODUCTION

Heat transfer in circular tubes in laminar flow is encountered in many engineering applications including, but not limited to heat exchangers, solar thermal collectors and boilers. For instance, in solar thermal collectors such as parabolic trough or linear Fresnel solar collectors, the heat transfer fluid, is usually heated in horizontal absorber tubes, for different applications ranging from hot water production to industrial process heat generation [1], etc. In this regard, Kalogirou and Lloyd [2] investigated the feasibility of a using parabolic trough solar collector for hot water production at 60°C for two applications - domestic and a hotel, compared with a flat plate solar collector for a low mass flow rate. They found that the parabolic trough is more efficient for large scale hot water production than the flat plate collector which is preferred for domestic installation due to it being relatively maintenance free. Kalogirou [3] also analysed the application of parabolic trough/linear Fresnel solar collectors for both steam generations and for make-up water pre-heating essential for many industrial process heating. Vyas *et al.* [4] analysed the thermal performance of two parabolic trough solar water heating experimental models with copper and aluminium absorber tubes respectively for laminar flow. They obtained water temperature rise from 20°C to 68.7°C with a copper tube and 20°C to 62.4°C with an aluminium tube, which indicates the essential application of the tubes in solar water heating.

The absorber tubes of these solar thermal collectors are usually subjected to non-uniform circumferential heating by the incident concentrated solar heat flux [5, 6], which could influence the heat transfer characteristics of the tubes, depending on the flow regime of the heat transfer fluid. Under the influence of gravitational field and non-uniform circumferential heating of the tubes, laminar flow mixed convection scenarios could occur where the buoyancy effects could become significant due to density differentials of the heat transfer fluid. Laminar and low mass flow rate cases are more specifically relevant to thermo-syphon driven systems, which rely on system-wide buoyancy driven flow to sustain fluid recirculation without the use of mechanically driven pumps.

Mixed convection effects could result in a severe departure from the well-known laminar velocity flow profiles of the heat transfer fluid and would thus, influence both the effective heat transfer coefficient as well as the friction factors differently under uniform and non-uniform circumferential heating of the tubes. However, investigations on the influence of non-uniform heat flux distribution boundaries on the internal heat transfers and friction factor characteristics of horizontal circular tubes are still lacking in the literature. Little to no information could be found that could be useful to thermal design engineers that could indicate buoyancy-induced secondary flow effects and the mixed convection heat transfer performance for non-uniform heat flux boundary cases. This could be due to the difficulties encountered when attempting to reproduce non-uniform thermal boundary conditions in an experimental set-up, or the complexity required when attempting to integrate the interaction between ray-tracing software and the numerical modelling software.

Due to a lack of information for non-uniform heat flux cases, it is interesting and relevant to consider the impact of mixed convection in general. A number of analytical [7,8],

experimental [9-12] and numerical [13-15] studies for horizontal circular tubes subjected to uniform heating boundary conditions, indicated that where mixed convection effects are present, the axial velocity, wall temperature profiles, the internal heat transfer coefficient and friction factors are significantly different from those of pure forced convection cases. Due to this situation, laminar flow mixed convection heat transfer cases need more specific attention. Shome [16] numerically investigated the effects of different fluid properties on mixed convection laminar flow and heat transfer in a uniformly heated smooth tube and found that an uncertainty of 10% for the fluid viscosity, thermal conductivity, density and specific heat could lead to an uncertainty of up to 5% and 8% for the predicted Nusselt number and friction factors. Prayagi and Thombre [17] performed a parametric study on buoyancy induced flow in circular pipes with uniform heat flux in a solar water heating system. Heat transfer correlations and flow characteristics were established for the buoyancy induced flow through inclined tubes. Laouadi *et al.* [18] numerically studied the effects of wall-conduction in externally uniformly heated pipes with fully developed laminar flow in terms of the secondary flow for horizontal and inclined orientations. They found that wall conduction increased the intensity of the buoyancy-driven secondary flow and that the flow patterns inside the inclined tubes are similar to that of horizontal tubes. Bernier and Baliga [19] also numerically investigated the effects of wall-conduction on laminar mixed convection in upward flows through pipes that are uniformly heated on their outer surfaces. They found that the wall conduction influenced the velocity and temperature profiles such that flow reversal occurred at the upstream entrance of the heated section. Sadik *et al.* [20] reported on different Nusselt number correlations for hydro-dynamical and thermal fully developed flow for combined free and forced convection heat transfer in horizontal and vertical circular tubes subjected to uniform wall heat flux conditions as well as uniform wall temperature boundary conditions. Ganesan, *et al* [21] experimentally investigated the effects of laminar flow mixed-

convection and surface-radiation heat transfer in a horizontal duct. They found that the surface temperatures were affected by the heat flux and emissivity of the walls, Reynolds number and length of the duct. They also found that for the same amount of heat flux, the surface temperature was higher at low Reynolds number flow and that the convective heat transfer rate was higher at higher Reynolds number flow due to the dominant effect of the forced convection at higher Reynolds number. Mixed convection has also been investigated for other geometries and it has been shown that the impact of buoyancy driven flow can be very significant. Ashjaee, *et al* [22] experimentally and numerically investigated local and average free convection heat transfer from a horizontal cylinder located above an adiabatic surface. They found that as the velocity of the fluid increased, the thermal boundary layer thickness decreased and that the local heat transfer rate increased at the lower surface of the cylinder. Karimi, *et al* [23] numerically investigated mixed convection around two heated horizontal cylinders located in the middle of a square enclosure with adiabatic walls. The study indicated that the heat transfer rate from the heated cylinders and the dimensionless fluid temperature in the cavity increased with an increase in the cylinder diameter and Richardson number. Yapici and Obut [24] numerically investigated laminar mixed-convection heat transfer in a square lid-driven with three different irregular bottom wall shapes: rectangular, triangular, and sinusoidal wave wall shapes. The cavity walls were heated from the bottom at constant different uniform temperatures. In that study, they found that at a low Richardson number (Ri = 0.01), the average Nusselt number increased linearly with the amplitude and that the rectangular wave shape gave the highest average Nuselt number followed by sinusoidal and triangular wave wall shapes. They also found that among other cases, the rectangular wave shaped wall gave the highest heat transfer rate.

Most of the prior investigations were based on either uniform wall heat flux or uniform wall temperature conditions. Only very few studies considered cases of partial uniform heat flux boundary conditions for laminar flow convection heat transfer, especially in horizontal circular tubes. Zeitoun [25, 26] performed a numerical study for fully laminar forced convection in partially heated tubes using the finite volume method. In their study, they investigated uniform heat flux and uniform temperature on the heated portion of the tube and assumed the remaining portion to be adiabatic. They found that the Nusselt number values increased as the tube wall thickness was increased and also increased with the decrease in the thermal conductivity ratio of the fluid and the tube. The variation in the Nusselt number obtained can be attributed to circumferential heat conduction effect in the tube wall which affects the average tube wall temperature. However, the influence of buoyancy-induced secondary flow and thermal losses by convection and radiation from the heated surface were not investigated. Lagana [11] noted that pure forced convective heat transfer rarely occurred in practical applications since buoyancy forces usually exist in any forced convection, even at low temperature differences. Patankar [27], in his well-known textbook included a numerical example of fully developed laminar flow and heat transfer in a horizontal tube subjected to partial uniform heating for two different circumferential heating conditions. In the first case, the top half of the tube was uniformly heated, while the bottom half was insulated, while in the second case, the opposite was considered. The results indicated that due to the buoyancy-induced secondary flow, the Nusselt number was much higher than those for pure forced convection without secondary flow and that the effect was more pronounced for the bottom-heating case. However, the example only considered the top half and bottom half circumferential uniform heating and neglected the convection and radiation heat flux losses from the heated tube surface. Also, some boundary conditions are not fully described in the

example, making it impossible for design engineers to make use of the published example solution for practical situations.

By default uniform wall heat flux or uniform wall temperature conditions result in heat flux distribution boundaries that are symmetrical in terms of the direction of gravity. Those investigation that did consider non uniform heat flux, only did so for symmetric distributions in terms of gravity. This is only applicable to solar collectors when the sun is at its zenith angle at approximately noon. This is represented in Figure 1(a) showing the cross section of a parabolic trough reflector and a collector tube. In this case the sun is at its zenith angle and the reflected heat flux is symmetrically distributed in terms of the direction of gravity (g). In case (b), this is not so. As the sun tracking system follows the sun during the day, the reflected heat flux becomes more and more asymmetric in terms of gravity. Little to no work has been done specifically to investigate the heat transfer and pressure drop characteristics of a horizontal solar collector tube when the sun is not at its zenith angle. This could significantly influence the thermal performance of the receiver absorber tubes, which play very critical roles in thermal energy conversion of a solar collector system. For instance, Stynes and Ihas [28, 29], in their studies noted that both the collector frame orientation and the absorber varied with respect to gravity as the parabolic trough solar collector tracks the sun from east to west throughout the day and this could result in misalignment of the absorber with the solar flux distributions on the focal line of the collector. They measured the absorber alignment through photogrammetry for different collector orientation angles to determine the gravitational effect on the absorber alignment. Similarly, Christian and Ho [30] used a finite element modelling and ray-tracing to determine the effects of gravitational loading on a parabolic trough solar collector, but the effects of gravity on the absorber alignment was ignored. Asymmetric heating studies for non-circular cross sections could be identified in the

literature [31-35], but because this is not very applicable to tube-based collectors, there is a need to investigate the impact of asymmetric heating in terms of gravity for circular collector tubes.

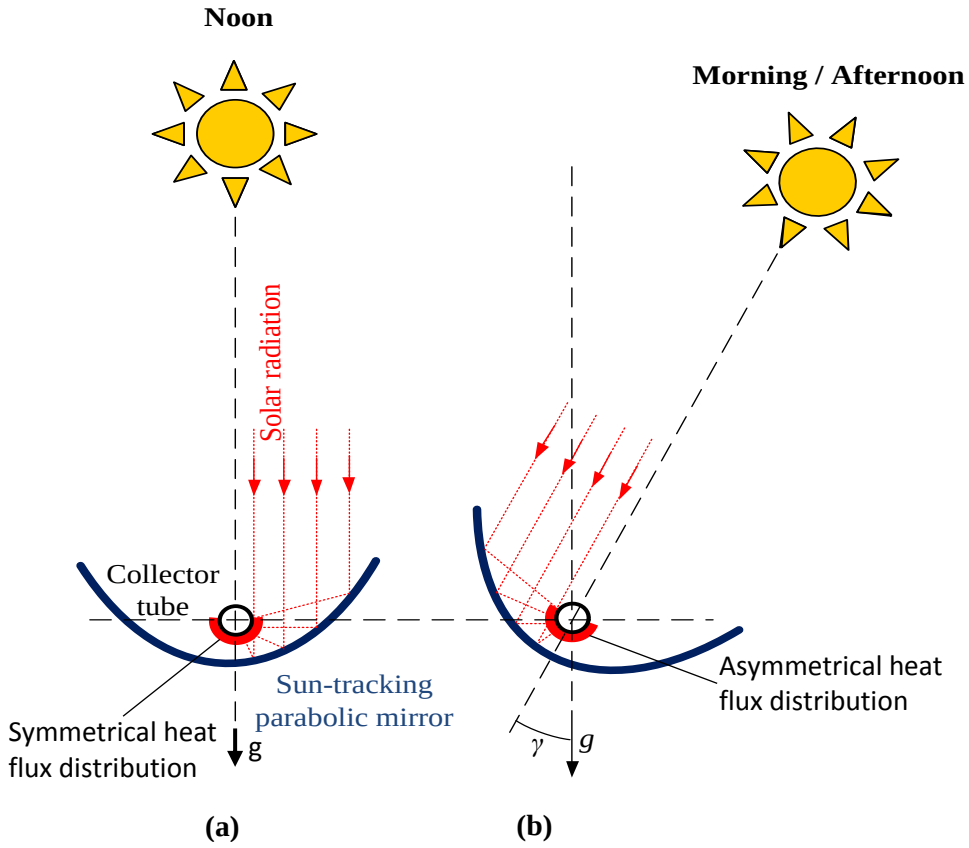

Figure 1 Parabolic trough solar collector with sun tracking system, indicating time-dependent misalignment of heat flux axis and the gravitational field for a) the sun at its zenith position and b) the sun at other positions

Purpose of Study

As shown, the impact of asymmetrical non-uniform heat flux distribution boundaries cases on heat transfer and fluid flow characteristics in the laminar flow mixed convection regime has not yet been adequately considered for horizontal circular tubes. Little information, other than that mentioned above, is available to thermal design engineers. It is also unclear what the influence of asymmetrical heating may have on the effective heat transfer coefficient for

horizontal circular tubes. Therefore in this study, the influence of asymmetric non-uniform heat flux boundaries on mixed convection heat transfer and friction factor characteristics in horizontal circular tubes are considered numerically for different circumferential angle spans of the heat flux distributions and degrees of gravitational asymmetry. The scope of this work is limited to single phase liquid water flow applicable in, for instance, parabolic trough or linear Fresnel solar thermal type collectors for pre-heating phases during hot water heat production at low mass flow rates.

PHYSICAL MODEL AND PROBLEM DESCRIPTION

The geometry of a stainless steel tube with a thermal conductivity of 16.27 W/mK is presented in Figure 2 and is intended to represent the collector tube in Figure 1. The tube has a total length of L_{TOT} = 10 m, an outer radius of R_o = 36.5 mm, and a wall thickness of t = 5.16 mm. This resulted in a length-to-inner diameter ratio (L_{TOT} /2R_i) of approximately 160. The dimension of the tube was according to the available commercial sizes. The length of 10 m was based on the LS-2 solar collector module. The tube-wall was divided into $M \times N$ number of sections in the axial and circumferential directions respectively. In this paper N = 36 was used with which the external heat flux boundary distribution are described.

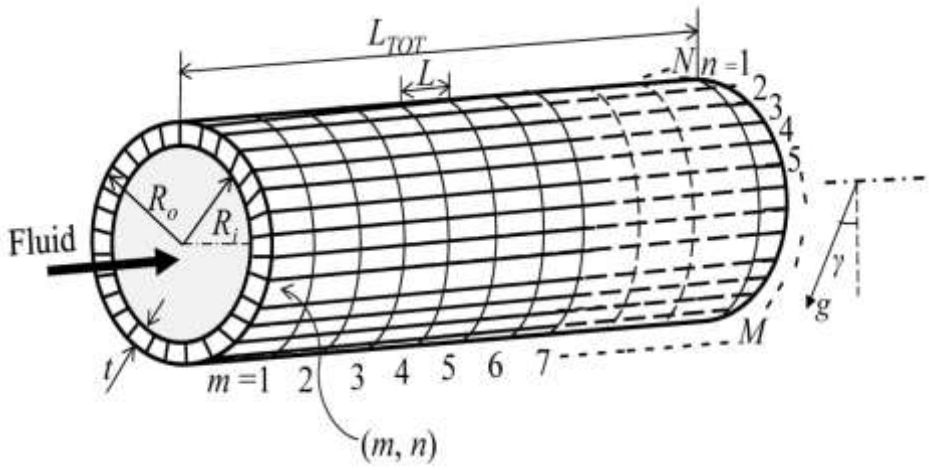

Figure 2 Tube model divided into M x N numerical surfaces

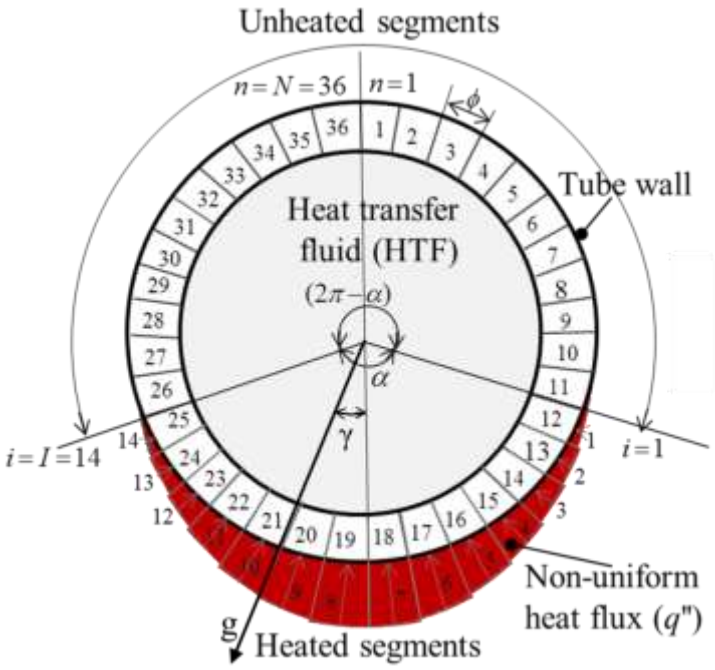

Figure 3 Cross-section of Figure 2 with sinusoidal non-uniform heat flux distributions and gravity (g) directed at angle γ

Figure 3 gives a cross-sectional view of the tube model presented in Figure 2, under the influence of the gravitational field at a misalignment angle of γ (°) with respect to the symmetry plane of the heat flux distribution. As the sun position changes from east to west during the day, the misalignment angle would change. When the sun is at its zenith angle, γ = 0°. The direction of gravity is for convenience represented in the same way as which it is taken into consideration in the numerical model. The heat flux distribution on the tube is such that the lower portion of the tube receives the maximum heat flux due to the presence of the parabolic reflector. The heat flux decreases upward on both sides of the tube towards the top portion and is dependent on the reflector geometry and the solar position. In Figure 3, an example of a non-uniform heat flux distribution considered in this paper is represented, and the numbering system (n = 1 to N, with N = 36) employed in simulating the non-uniform heat flux distributions around the tube is given. Of the N segments, only I number of segments receive external heat flux. It should be noted that the peak in the heat flux (at segment n = 18

and $n = 19$) does not necessarily match up with the gravitational direction, resulting in an asymmetric boundary condition in terms of the gravitational direction. The heat flux across the I number of segments that were heated was modelled based on a sinusoidal function of the heat flux distributions employed in our earlier study for the symmetric heated cases for turbulent [6] flow regime. The choice of this function could be linked to ray-tracing simulation results for the heat flux distributions such as those done by Wirz *et al*. [36] and Eck *et al*. [5], which demonstrated the non-uniform heat flux distributions for some solar collector applications. The use of a sinusoidal function is adopted in this paper since it approximately describes the expected heat flux distribution and is used merely here to emphasise the impact that the asymmetry has on the heat transfer and fluid flow characteristics of a collector tube. This distribution does not include any shadow effects which can be obtained from direct ray-tracing simulations. This would be dependent on the particular design and lay-out of a solar collector and falls beyond the scope of this paper. More information on the heat flux distributions used in this study is supplied later in this paper.

NUMERICAL FORMULATION AND HEAT TRANSFER MODEL

As mentioned, the wall was divided into N circumferential segments such that each had an angle span of ϕ :

$$\phi = \frac{2\pi}{N} \tag{1}$$

The angle span (in radians) of the heated and unheated portions of the tube are α and $2\pi - \alpha$ respectively (refer to Figure 3). The segment, in a clockwise fashion, where the heat flux distribution started, $n_{i=1}$, can be expressed in terms of α:

$$n_{i=1} = \frac{[N - I]}{2} + 1 \tag{2}$$

where n = 1, 2, 3... N , *and* i = 1, 2, 3... I. The number of segments of the tube model that were directly heated (with α being multiples of 20°), can be expressed as:

$$I = \frac{\alpha}{2\pi} N \tag{3}$$

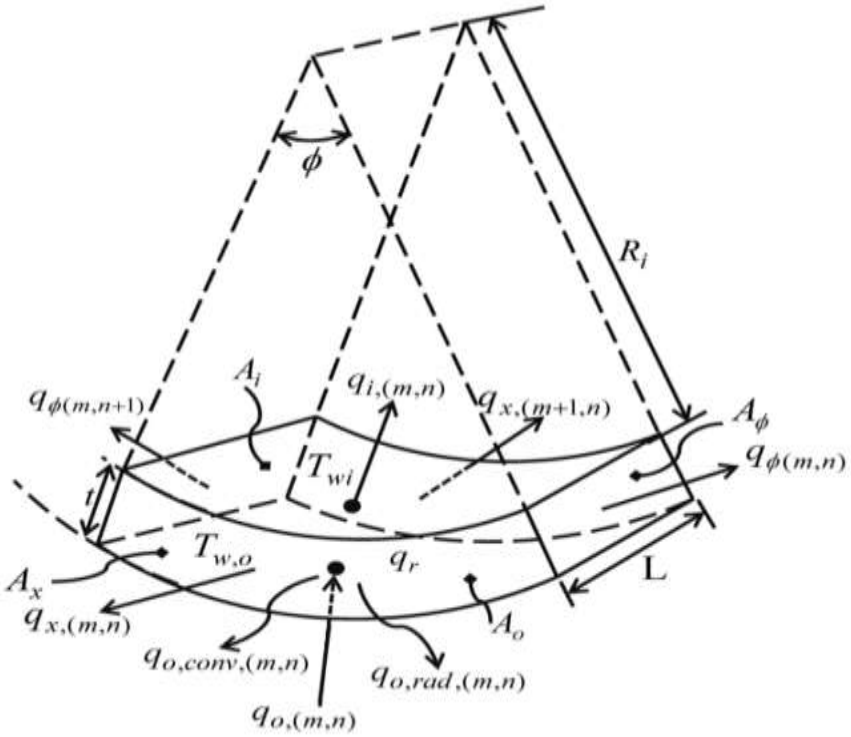

Figure 4 Control volume of the element

Figure 4 shows a control volume of the element at location (m, n). This control volume definition is used to describe the data-reduction method and how to interpret the heat transfer coefficient findings. The heat transfer components and dimensions t, ϕ and L, in the (x, r, ϕ) coordinate system are indicated. A_x and A_ϕ are the axial and tangential direction surface areas, while A_o and A_i are the external wall surface and the wetted internal wall surface areas of the element expressed in equations (4) and (5) respectively.

$$A_o = L.\phi.R_o \tag{4}$$

$$A_i = L.\phi.R_i \tag{5}$$

The heat transfer model under steady-state condition can be obtained, by applying the energy balance principle on the control volume element as follows:

$$q_{o,(m,n)} = q_{i,(m,n)} + q_{x,(m,n)} + q_{x,(m+1,n)} + q_{\phi,(m,n)} + q_{\phi,(m,n+1)} + q_{o,conv,(m,n)} + q_{o,rad,(m,n)} \tag{6}$$

Starting from left to right, each term in Eqn. (6) is briefly described next. $q_{o,(m,n)}$ is the incident heat transfer rate on the outer wall surface expressed in Eq. (7) as follows:

$$q_{o,(m,n)} = q''_{o,(m,n)} A_o \tag{7}$$

If the location is at the un-irradiated segment of the tube, then $q''_{o,(m,n)}$ was considered to be zero for purposes of this study. Next, $q_{i,(m,n)}$ is the heat transfer rate on the wetted surface to the working fluid which can be expressed as follows:

$$q_{i,(m,n)} = h_{i,(m,n)}.A_{i,(m,n)}(T_{wi,(m,n)} - T_{b,m}) \tag{8}$$

Here $h_{i,(m,n)}$ is the hypothetical local internal heat transfer coefficient, $A_{i,(m,n)}$ is the inner wall surface area, $T_{wi,(m,n)}$ is the inner wall temperature and $T_{b,m}$ is the fluid bulk temperature at the axial position m defined as:

$$T_{b,m} = T_{b,m-1} + \frac{\sum_{n=1}^{N} q_{i,(m,n)}}{\dot{m} c_P} \tag{9}$$

where $\dot{m}$ is the mass flow rate of the fluid and c_P is the bulk specific heat of the fluid. The average internal heat transfer coefficient $\bar{h}_{i,m}$ is related to the average Nusselt number as follows:

$$\overline{\mathrm{Nu}}_{i,m} = \frac{\bar{h}_{i,m} 2R_i}{k_f} \tag{10}$$

where $\bar{h}_{i,m}$ is the local circumferential average internal heat transfer coefficient at a specific axial position expressed as:

$$\bar{h}_{i,m} = \frac{\sum_{n=1}^{N} q_{i,(m,n)}}{2\pi R_i L\left(\bar{T}_{w,i,m} - T_{b,m}\right)} \tag{11}$$

$\bar{T}_{w,i,m}$ is the circumferential average local inner-wall temperature of the tube expressed as:

$$\bar{T}_{w,i,m} = \frac{1}{N}\sum_{n=1}^{N} T_{w,i,(m,n)} \tag{12}$$

The overall average internal heat transfer coefficient, $\bar{h}_i$ over the full length of the tube model in terms of the overall inner-wall surface temperature, $\bar{T}_{w,i}$ is expressed as follows:

$$\bar{h}_i = \frac{\sum_{m=1}^{M}\sum_{n=1}^{N} q_{i,(m,n)}}{2\pi R_i L_{TOT}\left(\bar{T}_{w,i} - \bar{T}_b\right)} \tag{13}$$

Returning to Eq. (6), the conductive heat transfers in the tangential direction, $q_{\phi,(m,n)}$ and $q_{\phi,(m,n+1)}$ are modelled with the Fourier law of heat conduction [37]. Also, in Eq. (6), $q_{x,(m,n)}$ and $q_{x,(m+1,n)}$ are the conductive heat transfers in the axial direction modelled from Fourier's law of heat conduction. $q_{o,conv,(m,n)}$ is the forced convective heat transfer loss from the outer-wall surface at (m, n) to the surroundings modelled from Newton's law of cooling [38] as:

$$q_{o,conv,(m,n)} = h_{o,(m,n)} A_o (T_{w,o,(m,n)} - T_a) \tag{14}$$

where $T_{w,o,(m,n)}$ is the outer-wall temperature at (m,n) and T_a is the ambient free stream air temperature. In this study, an ambient temperature of T_a = 303 K is used.

The external convective heat transfer coefficient, $h_{o(m,n)}$ related to the wind velocity, v_a *(m/s)* around the tube model is expressed as [39]:

$$h_{o(m,n)} = \bar{h}_o = 5.7 + 3.8v \tag{15}$$

In this study, v_a = 4.36 m/s to 18.24 m/s were used. The last term in Eq. (6), $q_{o,rad,(m,n)}$, represents the radiative heat transfer loss to the surroundings modelled with the Stefan-Boltzmann law of the emissive power of a surface at a thermodynamic temperature as follows:

$$q_{o,rad,(m,n)} = \varepsilon_{tu}\sigma_{SB}A_o(T^4_{w,o,(m,n)} - T^4_{\infty}) \tag{16}$$

where ε_{tu} is emissivity of the tube surface expressed in terms of the tube outer-wall temperature as follows: $\varepsilon_{tu} = 0.0003T_{w,o,(m,n)} + 0.3171$ [40] and σ_{SB} is the Stefan-Boltzmann constant ($5.67\text{x}10^{-8}$ W/m^2. K^4) [37]. T_∞ is the radiation temperature of the surrounding. In this study, a radiation temperature of T_∞ = 303 K is used.

Another important aspect to consider is the frictional pressure loss along the internal wall of the tube model. The friction factor, *f*, can be expressed in terms of the total pressure drop (ΔP) over the tube as [37]:

$$f = \frac{2R_i}{L_{TOT}}\frac{2}{\rho\bar{v}^2}\Delta P \tag{17}$$

where $\bar{v}$ is the mean fluid velocity.

The values of $\bar{h}_{i,m}$, $\bar{T}_{w,i,m}$, $\bar{h}_i$ and *f* in Eqs (11), (12) (13) and (17) were determined from the numerical simulation results obtained using ANSYS Fluent version 14.0 [41] for different circumferential angle spans of symmetrical (gravity directed at γ = 0°) and asymmetrical (gravity directed at γ = 20°, 30° and 40°) sinusoidal non-uniform heat flux distributions boundaries.

GOVERNING EQUATIONS

The governing equations for the heat transfer and fluid flow through the tube model were the continuity, Navier-Stokes and energy equations in cylindrical coordinates [20] presented as follows:

Continuity equation:

$$\frac{1}{r}\frac{\partial(rv_r)}{\partial r}+\frac{1}{r}\frac{\partial v_\phi}{\partial \phi}+\frac{\partial v_x}{\partial x}=0 \tag{18}$$

Navier-Stokes equations:

r-momentum:

$$v_r\frac{\partial v_r}{\partial r}+\frac{v_\phi}{r}\frac{\partial v_r}{\partial \phi}+v_x\frac{\partial v_x}{\partial x}-\frac{v_\phi^2}{r}=-\frac{1}{\rho}\frac{\partial p}{\partial r}+\frac{\mu}{\rho}\left[\nabla^2 v_r-\frac{2}{r^2}\frac{\partial v_\phi}{\partial \phi}\right]-g_r\Delta T\cos\phi \tag{19}$$

ϕ-momentum:

$$v_r\frac{\partial v_\phi}{\partial r}+\frac{v_\phi}{r}\frac{\partial v_\phi}{\partial \phi}+v_x\frac{\partial v_\phi}{\partial x}+\frac{v_r v_\phi}{r}=-\frac{1}{\rho}\frac{\partial p}{r\partial \phi}+\frac{\mu}{\rho}\left[\nabla^2 v_\phi+\frac{2}{r^2}\frac{\partial v_r}{\partial \phi}\right]+g_\phi\Delta T\sin\phi \tag{20}$$

x-momentum:

$$v_r\frac{\partial v_x}{\partial r}+\frac{v_\phi}{r}\frac{\partial v_x}{\partial \phi}+v_x\frac{\partial v_x}{\partial x}=-\frac{1}{\rho}\frac{\partial p}{\partial x}+\frac{\mu}{\rho}\nabla^2 v_x \tag{21}$$

$$\text{where}\quad \nabla^2\equiv\frac{1}{r}\frac{\partial}{\partial r}\left(r\frac{\partial}{\partial r}\right)+\frac{1}{r^2}\frac{\partial^2}{\partial \phi^2}+\frac{\partial^2}{\partial x^2}$$

Energy equation:

$$v_r\frac{\partial T}{\partial r}+\frac{v_\phi}{r}\frac{\partial T}{\partial \phi}+v_x\frac{\partial T}{\partial x}=\frac{k}{\rho c_p}\left[\frac{1}{r}\frac{\partial}{\partial r}\left(r\frac{\partial T}{\partial r}\right)+\frac{1}{r^2}\frac{\partial^2 T}{\partial \phi^2}+\frac{\partial^2 T}{\partial x^2}\right] \tag{22}$$

g is the acceleration due to the gravity vector, while v_r, v_ϕ and v_x are the radial, polar and axial velocity components respectively.

Assumptions

The fluid flow through the tube model was assumed incompressible and a three-dimensional steady-state laminar flow condition was considered for a single-phase liquid water with a uniform inlet velocity for the inlet Reynolds number range of 130 to 2000. Developing flow was considered since fully developed flow rarely occurs in practical applications. The density in the body force terms of the momentum equation in Eqs. (19) - (21) and that of the energy equation in Eq. (22) were considered temperature dependent for simulating buoyancy effects in the computational domain; however its temperature dependence was not specifically made part of the solution of the energy equation. Instead, the density value was updated once the temperature field was solved by using the Boussinesq approximation [41] to account for thermal expansion and contraction of the fluid as is specified in the next section. The effect of viscous dissipation was neglected.

BOUNDARY CONDITIONS AND MATERIAL PROPERTIES

The boundary conditions were as follows:

(i) Inlet boundary conditions (x = 0):

A uniform inlet velocity was used (uniform mass flux because the fluid is incompressible), since in practice the flows in pipes rarely have fully developed velocity distributions at the inlet. Unless stated otherwise, all variables were initiated with uniform values. The uniform values were based on the case under consideration:

$$\dot{m}_x(r,\phi) = \text{ 0.005 kg/s to 0.01 kg/s} \quad \text{and} \quad \dot{m}_r = \dot{m}_\phi = 0 \text{ kg/s} \tag{23}$$

$$T_f(r,\phi) = T_{b,0} = 300 \text{ K to } 360 \text{ K} \tag{24}$$

This range of mass flow rates covers a Reynolds number range of approximately 130 to 2000. This is not necessarily representative of the true laminar flow regime range. The critical Reynolds number for the start of the transition flow regime is dependent on a number of geometric and thermal parameters and the investigation there-off falls beyond the scope of this article. In the interest of completeness the results in this articles based on laminar flow assumptions are presented up to a Reynold number of 2000.

(ii) Outlet boundary condition ($x = L_{TOT}$):

A zero pressure gradient condition was applied across the outlet boundary, and the outlet pressure was set as follows:

$$P(r,\phi) = P_{atm} \tag{25}$$

(iii) Tube inner wall surface boundary condition ($r = R_i$):

No-slip conditions were applied at the inside absorber tube wall.

$$v_r = v_\phi = v_x = 0 \tag{26}$$

(*iv) External wall boundary conditions* ($r = R_o$):

The outer wall heat flux distributions considered in this paper are presented in Table 1. For the sinusoidal heat flux distributions, a base-level incident heat flux of q'' = 7.1 kW/m^2 is considered in this paper. The value of this heat flux will depend on for instance the solar radiation intensity and/or the concentration factor of the reflector system. The total amount of incident heat [W] in this paper is dependent on the total angle span, α, of the heated portion. For instance, for $\alpha = 160°$, the total incident heat is 4.6 kW for the given collector tube diameter and length, while for $\alpha = 360°$, the total incident heat is 10.3 kW. For comparison purposes, an associated fully uniform heat flux case are linked to each angle span case as defined in Table 1 such that it will have the same total incident heat transfer rate as the sinusoidal heat flux distribution case. This is done simply to allow the reader to relate the

results presented in this paper with prior result in literature which were obtained for fully uniform heat flux distributions.

Table 1 External surface heat transfer distributions types.

Heat flux distribution type		Outer wall incident heat flux	Wall element range
Sinusoidal non uniform heat flux cases:	Heated segment:	$q''_{o,(m,n)} = q'' \sin\left[\frac{\pi}{\alpha}\phi(n - n_{i=1} + \frac{1}{2})\right]$	$m \in [1, M]$ and $n \in [n_{i=1}, n_{i=1} + I)$
	Unheated segment:	$q''_{o,(m,n)} = 0$	$m \in [1, M]$ and $n \notin [n_{i=1}, n_{i=1} + I)$
Associated fully uniform heat flux cases:	All segments:	$q''_{o.(m,n)} = q'' \frac{\alpha}{\pi^2}$	$m \in [1, M]$ and $n \in [1, N]$

The thermal properties of the heat transfer fluid and tube material are presented in Table 2. All properties were assumed to be temperature independent except for the fluid density (ρ) and the fluid viscosity (μ). The density is expressed as a function of temperature using the Boussinesq approximation [41] in Eq. (27),

$$\rho = \rho_o[1 - \beta(T - T_o)] \tag{27}$$

Table 2 Properties of the heat transfer fluid and tube model material.

Property	Fluid (water)	Tube (stainless steel)
Density (ρ_o)[kg/m^3]	998.2	8030
Specific heat capacity [J/kgK]	4182	502.48
Thermal conductivity [W/mK]	0.61	16.27
HTF temperature (T_o) [K]	300	-

Here ρ_o is the operating density at the operating temperature of $T_o = 300$ K and β is the thermal expansion coefficient. The viscosity was temperature dependent according to the equation by Popiel and Wojtkowiak [42].

NUMERICAL PROCEDURE, GRID ANALYSIS AND MODEL VALIDATION

Eqs (18) – (22) were solved numerically using the finite volume method described by Ferziger and Perifi [43] and Patankar [27], implemented in ANSYS Fluent. The domain model in Fig. 2, which consists of the tube-wall and fluid, was meshed with Hex8 cells (hexahedron element with 8 vertices, 12 edges and bounded by 6 quadrilateral faces) and Wed6 cells (triangular prism element with 6 vertices, 9 edges, bounded by 2 triangular and 3 quadrilateral faces) grid structures using the grid generation tool of the ANSYS Workbench. Hexahedral meshes generally give highest solution accuracy, while the triangular prism mesh resolves the boundary layers very efficiently [41]. The convective terms in the Navier-Stokes and energy equations were discretised and solved using a second-order upwind scheme and the standard SIMPLE algorithm was used for the pressure-velocity coupling. The boundary conditions and material properties specified in the ANSYS Fluent were modified to suit the present study. The pressure-based solver was employed and a decrease in the residuals to 10^{-3} for continuity and momentum equations and to 10^{-6} for energy equation is generally the least qualitative convergence for this solver. Thus, the convergence criteria for the continuity, momentum and energy equations were set such that the maximum residual values had to be less than 10^{-6} and 10^{-8} respectively. The incident heat flux boundary conditions in Table 1 and the convective and radiative heat losses in Eqs (14) and (16) were implemented according to the angular position of the boundary element via user-defined functions.

A series of grid dependence studies were carried out at different mass flow rates in terms of the outlet temperature rise of the heat transfer fluid for laminar flow regime at an inlet

Reynolds number range of 130 to 2000. It was ensured that the grid was sufficiently fine in order not to have any significant effect on the numerical results. For demonstration purposes, the mesh refinement results for the case of an inlet Reynolds number of 202 are presented in Table 3. Also, a grid dependence study in terms of the Grashof number is presented in Figure 5 for an inlet Reynolds number range of 130 to 2000, indicating insignificant effect of the grid cells on the buoyancy driven flow as the grid cells were refined by increasing the number of cells from 145 866 to 540 108 cells.

Table 3 Grid refinement test results.

Number of numerical cells	Bulk fluid outlet temperature[K]	Change in temperature due to refinement
145 866	397.4844	-
465 854	397.3815	0.102
481 327	397.3763	0.005
508 028	397.3747	0.002
525 147	397.3648	0.009
540 108	397.3563	0.008

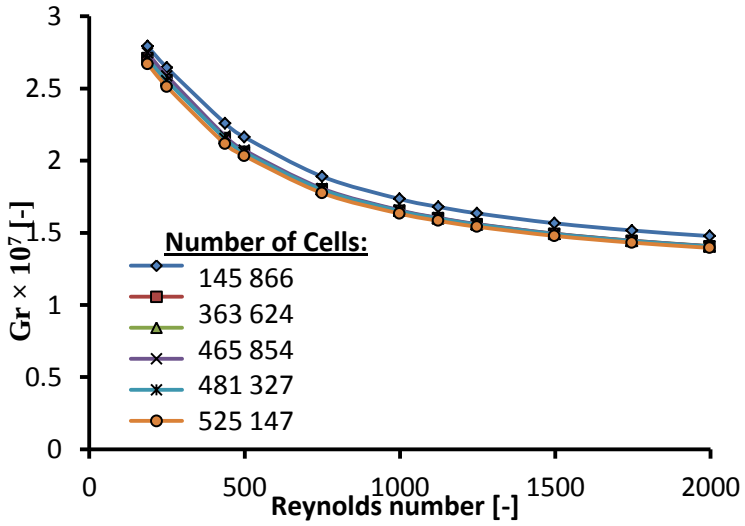

Figure 5 Grid dependence study in terms of Grashof (Gr) number

Because no work specifically on non-uniform heat flux condition could be obtained from literature, the validations of the model were mostly based on uniform heat flux data and correlations, and on limited implied non-uniform data.

The model was validated by first comparing the axial local Nusselt number determined from the simulation results, with the analytical expression, Nu_{Di} = 4.364, in [37] for a 360° span of uniform heat flux at inlet Reynolds number of 202, when the fluid density was considered independent of temperature. Figure 6 shows the results for the axial local Nusselt number obtained using Eq. (11) for the numerical simulation results compared with that of the analytical expressions. It was found that the numerical results were in good agreement with the analytical expression as the flow became more fully developed towards the exit of the tube.

The model was also validated for mixed convection with buoyancy driven flow based on Eq. (27). A comparison was made between the numerically obtained axial local Nusselt number and that of the Nusselt number correlations published by other researchers. These correlations are the Shah correlation [44] in Eq. (28) and an experimental correlation [45] in Eq. (29) for the laminar flow mixed convection under uniform heat flux boundary conditions.

$$\mathrm{Nu}(x) = \left[4.364^3 + 1 + \left(2.117 \left(\mathrm{Re}\,\mathrm{Pr}\frac{2R_i}{x} \right)^{1/3} - 0.6 \right)^3 \right]^{1/3} \tag{28}$$

$$\mathrm{Nu}(x) = 1.953 \left(\mathrm{Re}\,\mathrm{Pr}\frac{2R_i}{x} \right)^{1/3} \quad \text{for} \quad \mathrm{Re}\,\mathrm{Pr}\frac{2R_i}{x} \geq 33.3 \tag{29}$$

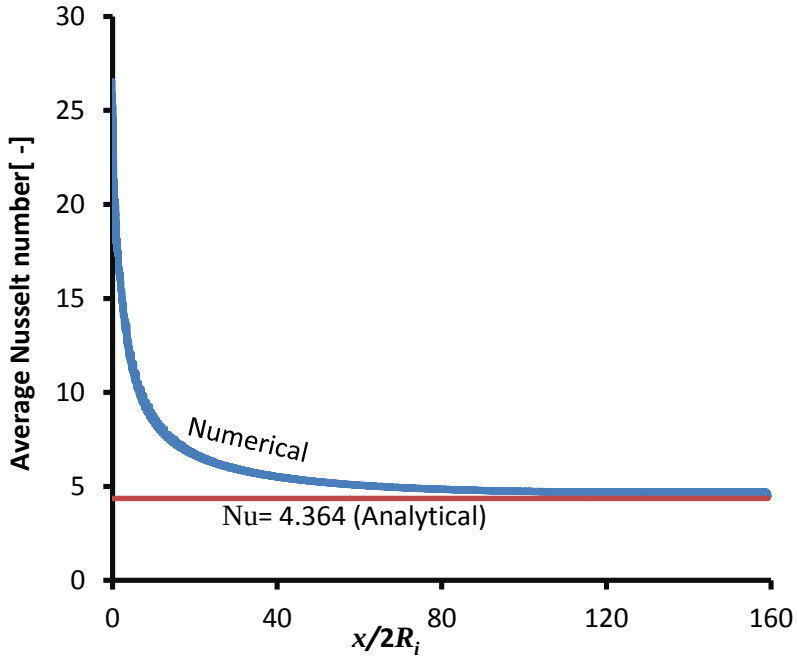

Figure 6 Axial local Nusselt number for numerical and analytical expression an inlet Reynolds number of 202

The model validation results are presented in Figure 7. The axial local Nusselt number values obtained from the numerical results are compared with the Nusselt number values from Eqs. (28) and (29). It indicates that the axial local Nusselt number obtained from the numerical results is in good agreement with the experimental correlations. The numerical results deviated by 18% from the correlation in Eq. (28) and by 15% from the correlation in Eq. (29) at $x/2R_i \approx 30$ and the errors further decreased to 10% and 3% at $x/2R_i \approx 160$ respectively as the flow, became more developed down the tube length. These differences could be due to mismatched thermal boundary conditions used for the correlations and this study, and also due to the buoyancy effects which we will show in this paper is dependent on the wall thermal boundary conditions, as is also allured to by Ghajar and Tam [46]. Note that these correlations do not yet take into consideration the impact of asymmetric non-uniform heat flux conditions.

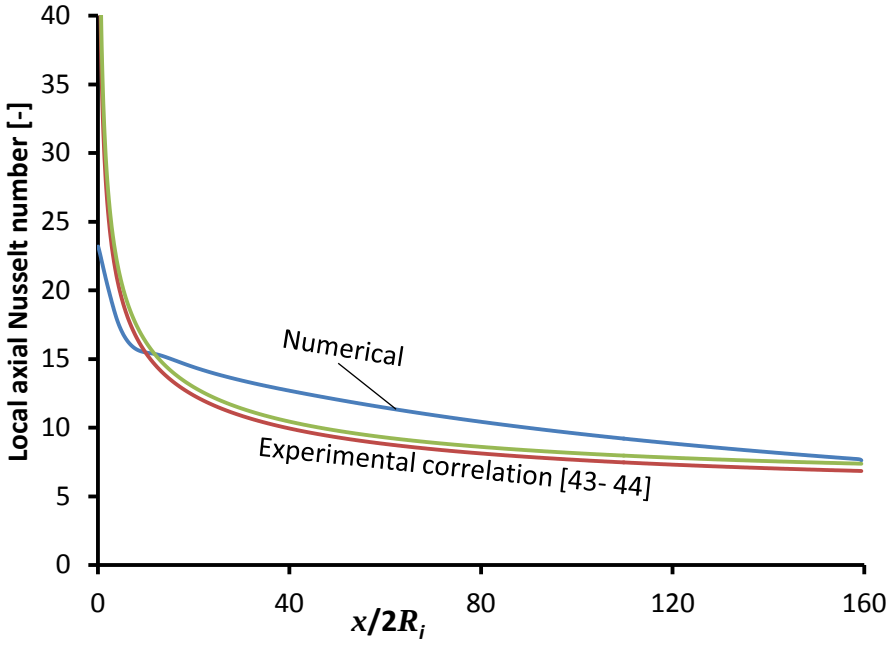

Figure 7 Axial local Nusselt number for numerical and experimental correlations at an inlet Reynolds number of 750

The model was further validated by comparing the efficiency of a solar collector and the heat loss from experimental results of the SANDIA final test on Schott's heat collector element (HCE) placed on a LS-2 solar collector module [47], under symmetrical heat flux boundary and that obtained from the present numerical simulation model. The Schott's HCE consists of an absorber tube with outer diameter of 0.07 m and glass tube cover with outer diameter of 0.125 m and vacuum in the annulus to minimize convection heat loss. The data used for the model validation are in Table 4. The Syltherm 800 liquid oil was used as the heat transfer fluid and the thermal properties were obtained from [48]. As it could be expected, the collector efficiency decreased as the heat losses increased with an increase in the fluid temperature due to increase in convection, conduction and radiation heat losses. Figures 8 and 9 show that the model results, the experimental tests results and that of the curve fit for LS-2/ UVAC2 HCE respectively are in good agreements and most of the values for the case of the collector efficiency are within the experimental error bars of 3%. However, the model

results over-predicted the collector efficiency. In Figure 8, the model results for the heat loss and that of the curve fit for LS-2/UVAC2 HCE indicated some discrepancies with the experimental results within the error bars of 10% especially at the higher operating temperature. The discrepancies could due to variation of the optical properties of the HCE with temperature, the uncertainty in measuring small temperature change across the HCE, the assumptions of negligible heat conduction at the ends of HCE, possible misalignment between HCE and the collector [49] and the uncertainties due to the thermal properties of the heat transfer fluid and the empirical correlations used in determining the heat transfer coefficients.

Table 4 Parameters of the Schott's HCE placed on the LS-2 Solar Collector module [47] used for the model validation.

Parameter	**Value**
Ave. Normal incidence pyrheliometer reading	934.30 – 1051.08 W/m^2
Ave. Wind speed	3.1 – 13.8 miles per hour
Concentrator length	7.8 m
Collector aperture	5 m
HCE length	4 m
Ave. ambient temperature	3.52 – 14.67 °C
Average flow rate	9.95 – 14.68 gal/min
Absorber inner diameter	0.066 m
Absorber outer diameter	0.070 m
Glass inner diameter	0.109 m
Glass outer diameter	0.12 m
Receiver absorptance	0.96
Glass transmittance	0.935
Selective coating emissivity	$\varepsilon = 0.000327\,T - 0.065971$
Incident angle	0^o

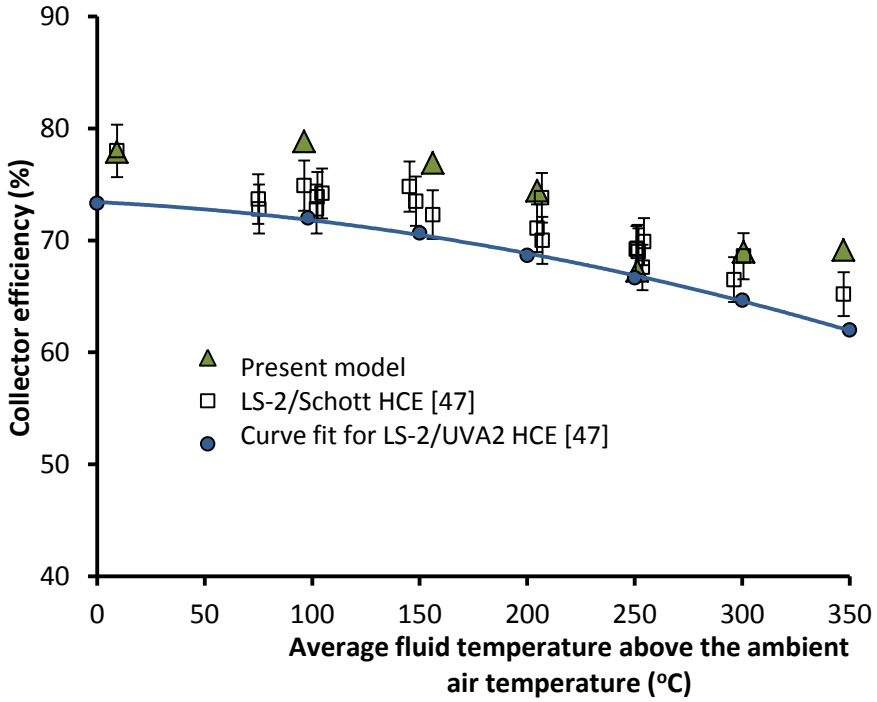

Figure 8 Variations of the efficiency of a solar collector with the average fluid temperature above the ambient air temperature

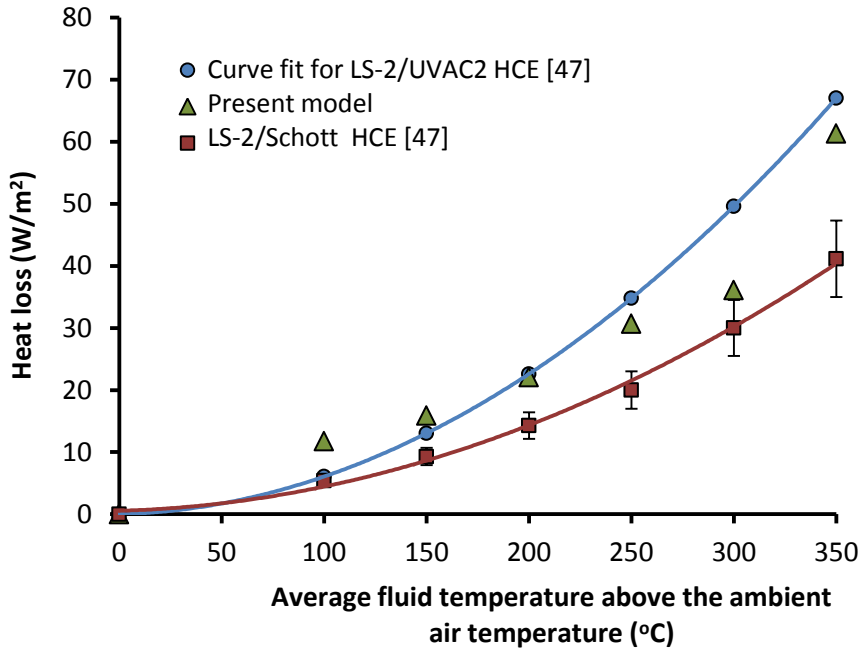

Figure 9 Variations of the heat loss from a solar collector with the average fluid temperature above the ambient air temperature

RESULTS AND DISCUSSION

Temperature Contour for Asymmetrical Non-Uniform Heat Flux Distributions

Figure 10 shows the converged temperature contours for different angle spans for γ = 30°. The temperature contours show asymmetrical non-uniform temperature profiles over the circumferential outer wall surface of the tube linked to the asymmetric nature of the heat flux distribution. It was found that the outer-wall surface temperatures increased in the flow direction as expected, and was the highest with the larger angle spans. Highest temperatures were obtained on the lower portions of the tube which coincided with the peak heat flux levels.

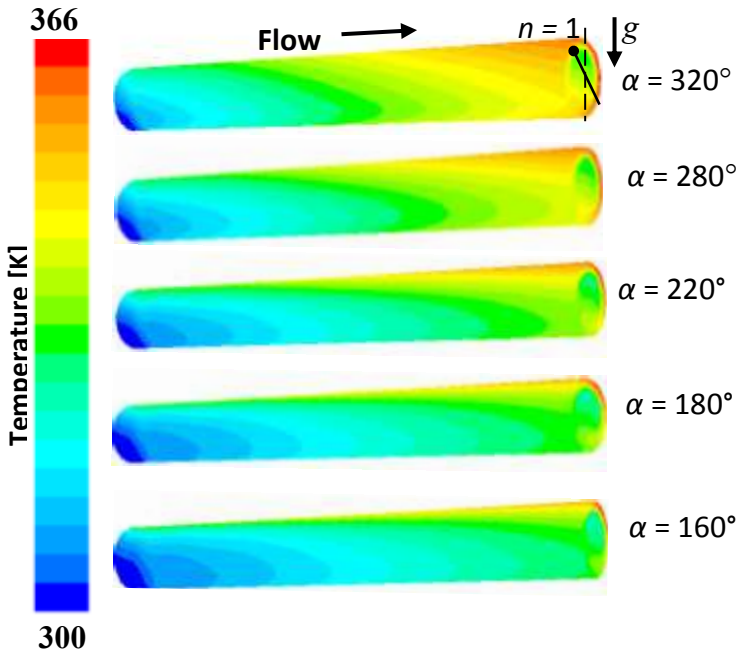

Figure 10 Temperature contours for different angle spans of asymmetrical sinusoidal non-uniform heat flux distributions for γ = 30°

The non-uniformity of the tube-wall temperatures for the asymmetrical heat flux case in Figure 10 is also demonstrated in Figure 11, where the non-uniform temperature factor, θ, given in Eq. (30) is plotted against the circumferential position (n) for different α values.

Figure 11 is based on the average outer surface temperature of the full axial length-wise of the tube model. θ is essential in determining the non-uniform tube-wall temperature distributions due to non-uniform circumferential heat flux distributions over the circumferential outer surface of the tube model.

$$\theta = \frac{T_{w,o,(n)} - T_b}{\overline{T}_{w,i,(n)} - T_b} \tag{30}$$

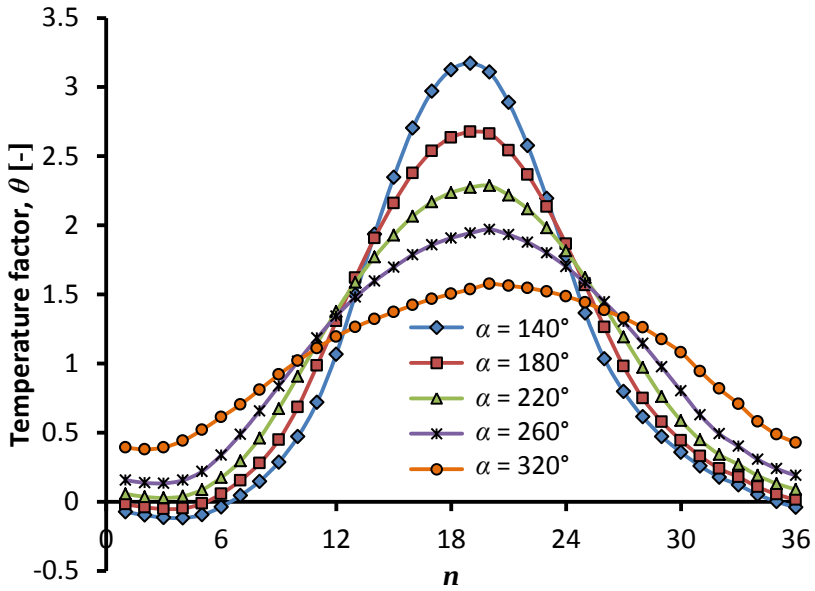

Figure 11 Non-uniform tube wall temperature factors for different angle spans of asymmetrical non-uniform heat flux boundaries for γ = 30°

Here $T_{w,o,(n)}$ is the local outer-wall temperature of the tube for segment n, T_b is the local bulk fluid temperature and $\overline{T}_{w,i,n}$ is the local average circumferential inner-wall temperature:

$$\overline{T}_{w,i,n} = \frac{1}{N}\sum_{n=1}^{N} T_{w,i,(m,n)} \tag{31}$$

Figure 11 shows that peak θ values decreased with an increase in the angle span. The regions with low θ values correspond to the region of tube with no incident heat flux, while those

regions with high θ values correspond to the region of higher heat flux. Each angle span profile should be viewed as a whole. The wider the range of θ, the more non-uniform the circumferential wall temperatures are. Thus, it can be seen that the larger angle span cases had lower degrees of non-uniformity in the tube wall temperature. When $\theta = 0$, it indicates that both the inner-wall and outer-wall had the same temperature, or that the outer wall temperature was equal to the bulk fluid temperature. This is an indication that little to no overall radial heat transfer occurred at that location. However, for $\theta > 0$, it indicates that there was significant heat transfer from the outer-wall to the fluid. It can also observed in Figure 11 that towards $n \approx 1$ and $n \approx 36$, θ is smaller for smaller heat flux angle spans. This indicates less heat transfer from the outer-wall to the fluid at such locations.

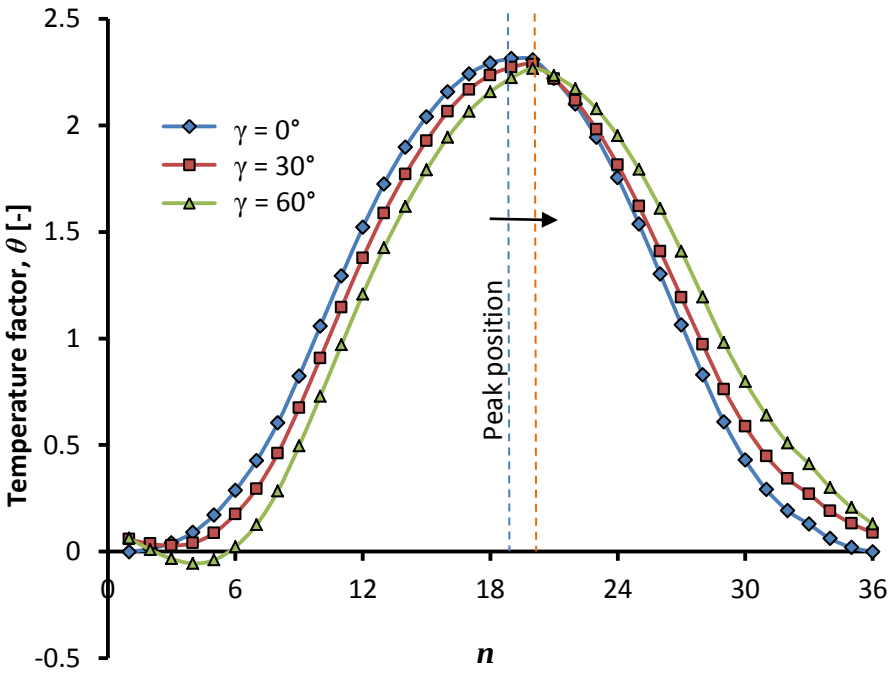

Figure 12 Non-uniform tube wall temperature factors for an $\alpha = 220°$ span at different asymmetries

Figure 12 shows the non-uniform wall temperature factor profiles for $\alpha = 220°$. It can be seen that the temperature factor only slightly deviated from that of the symmetrically heated case (gravity directed at $\gamma = 0°$). When $\gamma = 40°$, the maximum non-uniform temperature factor

shifted away from $n \approx 18$ to 19, to $n \approx 20$ to 21. This deviation could significantly influence the internal heat transfer characteristics of the tube model as will be shown in sections that follow.

Fluid Flow Velocity and Temperature Distributions

Figure 13 shows the in-plane velocity distributions in the heat transfer fluid as well as the temperatures at the outlet for different inlet Reynolds numbers with $\alpha = 220°$ and $\gamma = 0°$. The velocity vector arrows indicate the upward moving buoyancy-driven flow of the less dense fluid and the downward moving momentum-driven flow of the denser fluid due to influence of the gravity field. It can be seen that the denser fluid descends to the lower region of the tube along the vertical centre of the tube, while the less dense fluid ascends along the tube inner-wall. This was due to the temperature gradient which created the instability that resulted in the counter-rotating vortices that are superimposed on the forced convection flow, as also reported in [15, 20 and 46]. The overall effect of this phenomenon is an improved mixing of the heat transfer fluid and hence increases the heat transfer rate in laminar flow which are generally characterised by low heat transfer coefficient compared with turbulent flow. It can also be seen that the intensity of the upward and downward circulations of the fluid decreased with the increase in Reynolds number. This indicates that the influence of the buoyancy effects in laminar mixed convection decreases with an increase in forced convection effects. Figure 13 also indicates that the temperature distributions in the fluid varied due to buoyancy effects. It can be observed that the temperature of the tube and that of the fluid near the heated wall were higher than the temperature of the fluid towards the inner region of the tube. The red shade near the heated inner-wall shows the less dense fluid layers with higher temperature. The fluid with higher temperature circulated towards the upper regions of the tube.

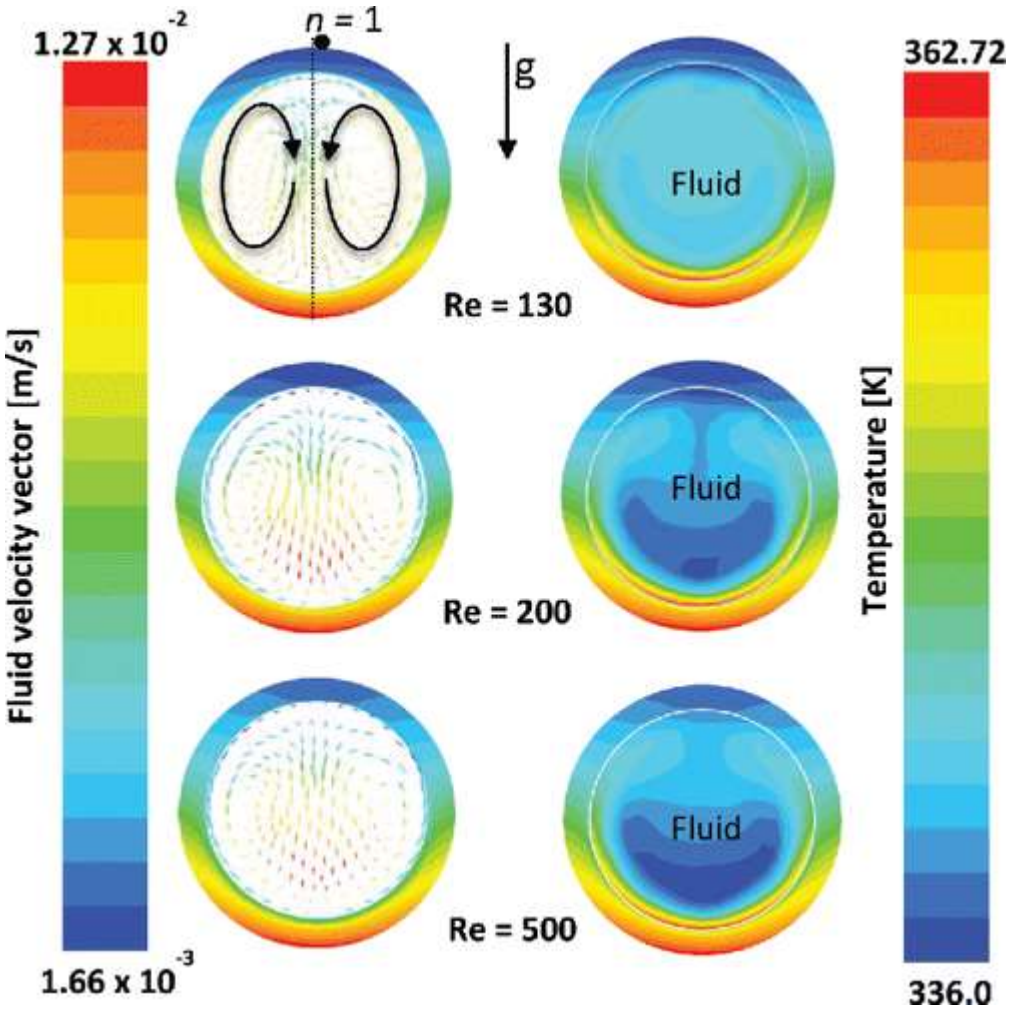

Figure 13 Fluid flow velocity and temperature distribution in the fluid for an α = 220° span and γ = 0°

Figure 14 shows the in-plane velocity and temperature distributions at the outlet of the tube for α = 220° and γ = 30° at different inlet Reynolds numbers. Unlike in Figure 13, it can be seen that the fluid descending to the lower region of the tube had shifted away from the heat flux symmetry plane. This situation could retard the upward and downward circulations of the fluid and could impede the effective mixing of the fluid and thus a decrease in the internal heat transfer rate. The intensity of the downward and the upward circulations of the denser and less dense fluid also decreased with an increase in the Reynolds number similar to as in the symmetrical case. Unlike in Figure 13, the fluid temperature layers are slanted due to the

misalignment of the non-uniform heat flux boundary and the gravity field. It also shows that the temperature of the fluid near the heated lower region of the tube was significantly higher than the temperature of the fluid towards the inner region of the tube and that the coldest fluid temperature region occurred slightly above the heated tube wall.

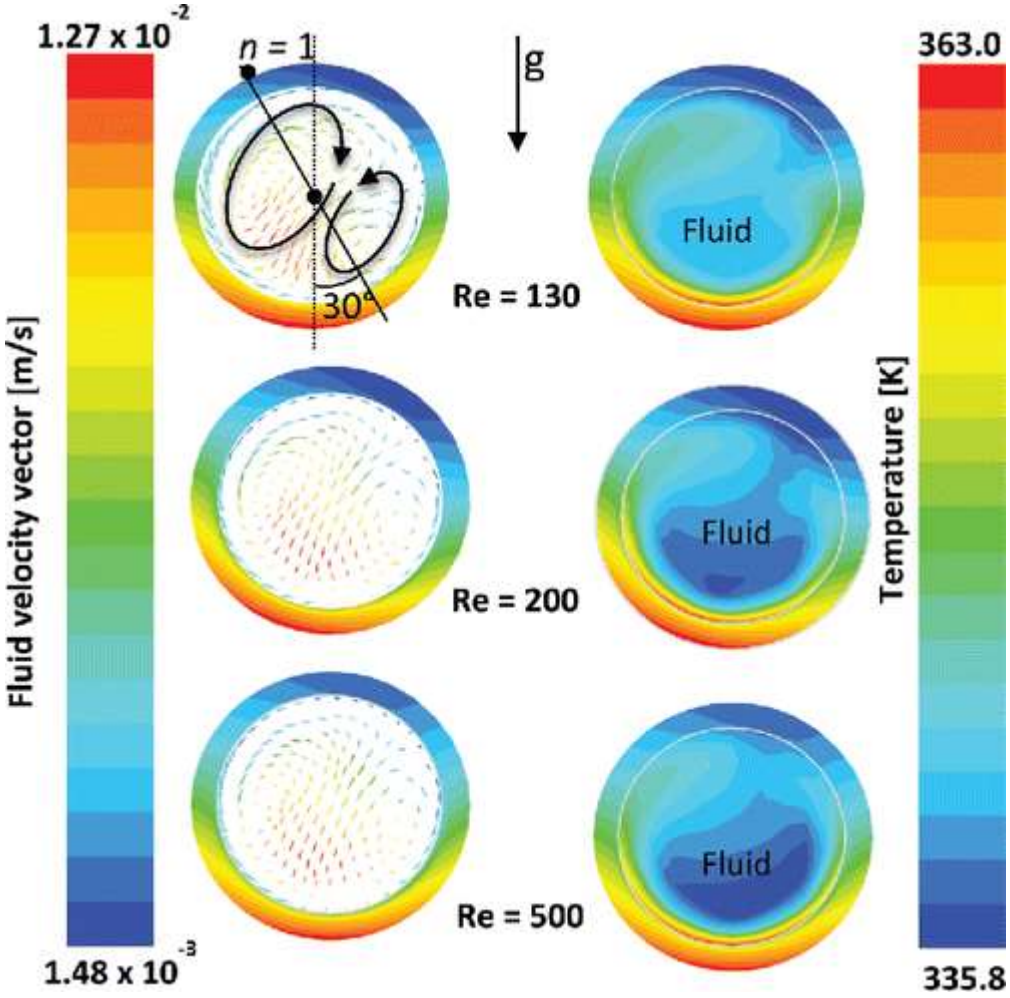

Figure 14 Fluid flow velocity and temperature distribution in the fluid for an α = 220° span and γ = 30°

Richardson Number

The Richardson number (Ri), given in Eq. (32) in term of the Grashof and Reynold numbers, indicates the strength of the natural convection due to buoyancy-induced secondary flow relative to forced convection.

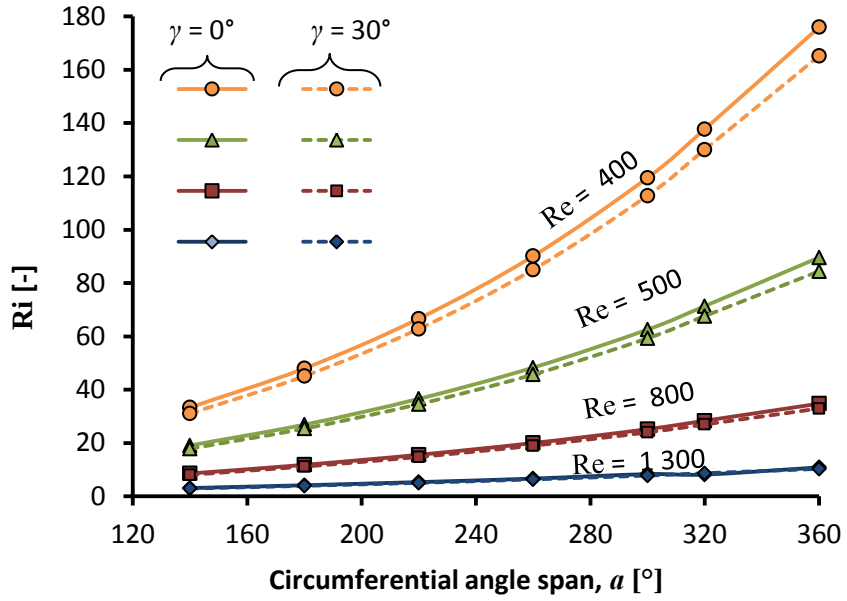

Figure 15 Variation of Ri with different angle spans of symmetrical and asymmetrical heat flux case types

$$\mathrm{Ri} = \mathrm{Gr} / \mathrm{Re}^2 \tag{32}$$

If Ri >10, forced convection is considered negligible, while if Ri < 0.1, natural convection is negligible. If 0.1< Ri <10 both natural and forced convection are significant [37]. Figure 15 shows the variation of Richardson number at different circumferential spans for symmetrical (γ = 0°) and asymmetrical (γ = 30°) sinusoidal non-uniform heat flux case types at different inlet Reynolds numbers. The symmetrical case types are shown in solid lines while asymmetrical case types are shown with broken lines. For both case types, Ri increased with an increase in the circumferential surface of the tube exposed to the incident heat flux and thus an increase in the effective heat input rate into the tube. It was found that Ri for the symmetrical case was approximately 6 – 7% higher than that of asymmetrical case for the Reynolds number cases considered. This revealed that the influence of buoyancy-induced secondary flow decreased when there was misalignment between the gravity field and the heat flux symmetry plane. For all the cases considered at *Re* = 400 and *Re* = 500, Ri was

greater than 10, which indicates that the heat transfer was dominated by natural convention due to buoyancy effect and that forced convection effect was negligible. For some Re = 800 cases (α = 260° to 360°) and all Re = 1 300 cases, Ri was found to be between 0.1 and 10, which indicates mixed convection states.

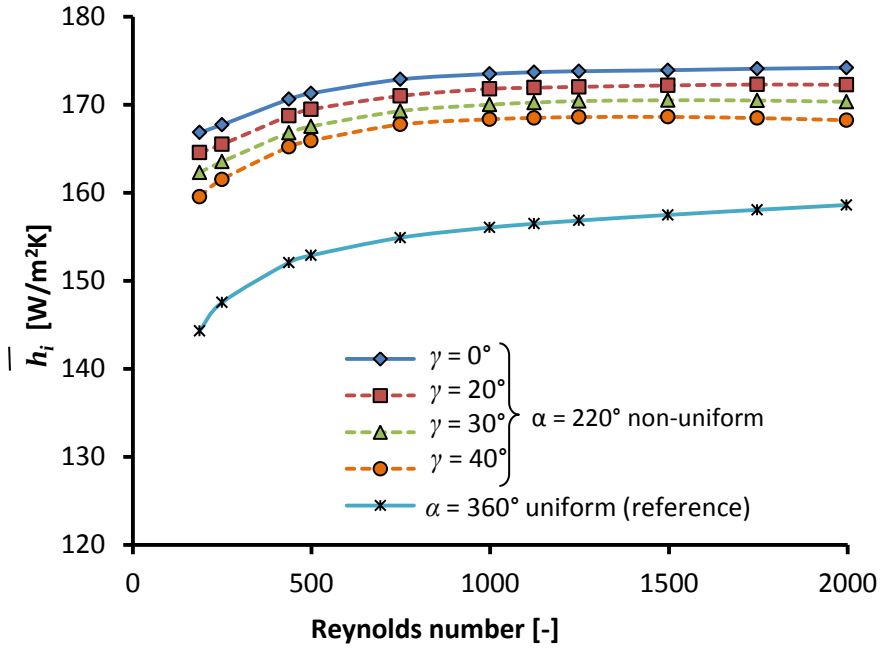

Figure 16 Average internal heat transfer coefficients for non-uniform heat flux distribution at α = 220° and different values of γ compared to the associated uniform heat flux distribution

Heat Transfer Coefficients

Figure 16 shows the variation of the average internal heat transfer coefficient for α = 220° at γ = 20°, 30° and 40° for the non-uniform heat flux distributions at different inlet Reynolds numbers. Also included in this figure, for comparative purposes, are the heat transfer coefficients for the associated fully uniform heat flux case (see Table 1). All results in this figure are thus for tube cases having the same incident heat transfer rate [W] on the outer tube wall. The fully uniform heat flux case distributes the heat evenly, while the non-uniform sinusoidal heat flux distributions result in higher heat flux concentrations over a smaller outer tube surface as shown in Figure 3. Symmetrical heat flux cases are represented with solid

lines while asymmetrical cases are represented with the broken lines. It can be seen that the misalignment between the heat flux symmetry plane and the gravity field has a significant influence on the average internal heat transfer coefficient. It can be seen that the heat transfer coefficient decreased as γ increased. For all the cases contained in Figure 16 it was, however, found that concentrated non-uniform heat flux cases described by the sinusoidal type function had higher effective heat transfer coefficients than the associated uniform heat flux case, even though the same incident heat transfer rate was applied. This could be due to differences in buoyancy-induced secondary flow and the relative sizes of the circulation vortices, indicating that appropriate heat flux distributions boundary must be considered; otherwise the internal heat transfer coefficient would be underestimated if uniform heat flux is considered where the actual heat flux distribution boundary is non-uniform. The average internal heat transfer coefficient for the symmetrical case (γ = 0°), was 1.4%, 2.7% and 4.3% higher than that of the asymmetrical cases of γ = 20°, 30° and 40°, and 13% higher than the associated uniform heat flux case, all at a Reynolds number of 187. It can also be observed in Figure 16 that for the non-uniform heat flux cases the heat transfer coefficient decreases slightly at higher Reynolds numbers. This is due to decrease in the effective buoyancy-effect with Reynolds numbers. In Figure 15, buoyancy-effects also decrease with an increase in Reynolds number and a decrease in Richardson number due to an increase in forced-convection effect. Figure 15 also indicates that the buoyancy effect decreases with an increase in γ.

Figure 17 shows the influence of different circumferential spans of the sinusoidal non-uniform heat flux distributions at different inlet Reynolds numbers on the average internal heat transfer coefficient. The figure allows the average internal heat transfer coefficients to be compared with the cases where the sinusoidal non-uniform heat flux distributions were symmetrical (γ = 0°) and asymmetrical (γ = 30°). It was found that the average internal heat

transfer coefficient for the asymmetrical case was lower than that of the symmetrical case for all angle spans. These differences were higher for larger angle spans. The average internal heat transfer coefficient for the symmetrical case was found to be marginally higher by approximately up to 3.0% across the Reynolds number range considered.

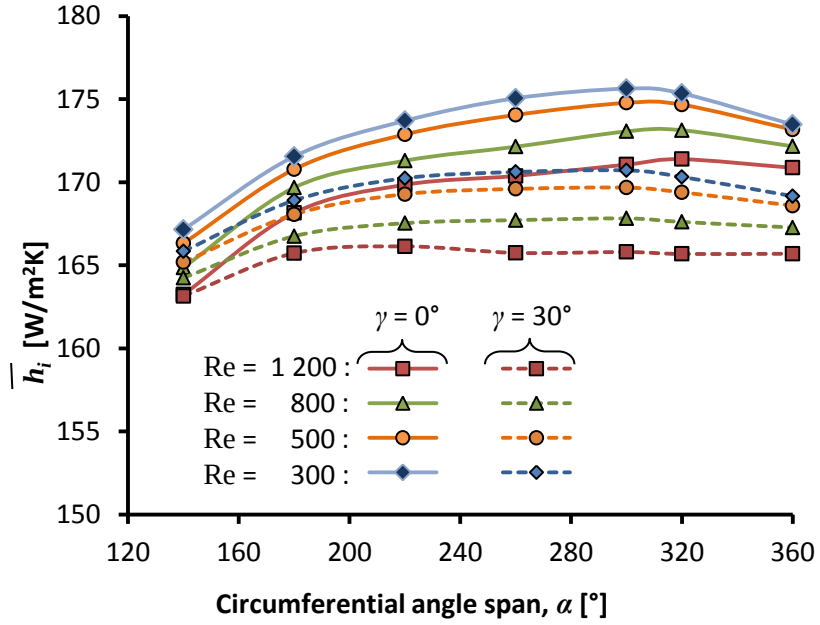

Figure 17 Average internal heat transfer coefficient for different angle spans of symmetrical and asymmetrical heat flux distributions

Figure 18 shows the variation of average axial local internal heat transfer coefficients over the tube for symmetrical and asymmetrical cases with α = 320° for an inlet Reynolds number of 750. The figure also compared the average axial local internal heat transfer coefficients with and without buoyancy-induced secondary flow. In both cases, the heat transfer coefficients were found to be higher at the inlet of the tube where the thermal boundary layer was thinnest. As the thermal boundary layer increased and the flow became more developed, the heat transfer coefficient decreased with an increase in the length-to-inner diameter ratio of the tube. The decrease is due to the decrease in the axial local Richardson number with a decrease in the buoyancy-induced secondary flow effects along the tube length and that the

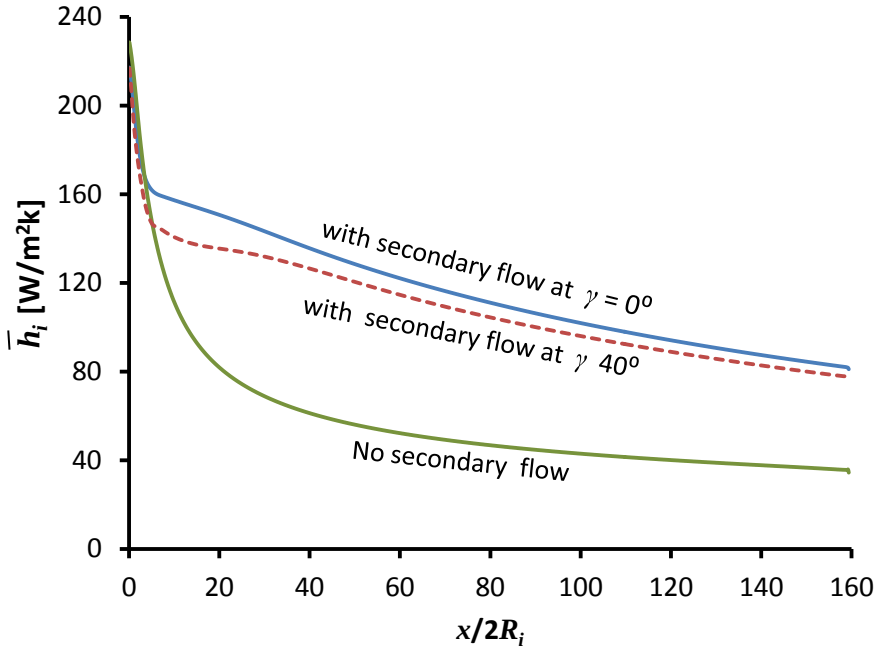

Figure 18 Axial local heat transfer coefficients for symmetrical and asymmetrical non-uniform heat flux distributions for an inlet Reynolds number of 750

expected fully developed flow at *L/D* = 40 for Re = 800 could rarely occur in a real flow application through the tube model. It can be observed that at the hydrodynamic and thermal inlet region of the tube, heat transfer coefficient coincided, indicating no significant influence of buoyancy effect, due to low temperature gradient. However, as the flow continued downstream, the buoyancy effect dominated the forced-convection effect and heat transfer coefficient became higher. Thus, the heat transfer coefficient for the case with secondary flow was found to increase from 15% to 125% for γ = 0° and 11% to 120% for γ = 40°, higher than that without secondary flow at $x/2R_i \approx 10$ to $x/2R_i \approx 105$, respectively. This variation indicates that the internal heat transfer coefficient would be underestimated if buoyancy-effects were neglected. It was also found that the average local axial internal heat transfer coefficients for the symmetrical (γ = 0°) case was up to approximately 6.0 % higher than that of the asymmetrical (γ = 40°) case. This implies, for instance, that the thermal performance for an absorber tube of a solar collector would be adversely affected when the

receiver absorber tube misaligned with the solar flux distributions incident on the focal line of the collector.

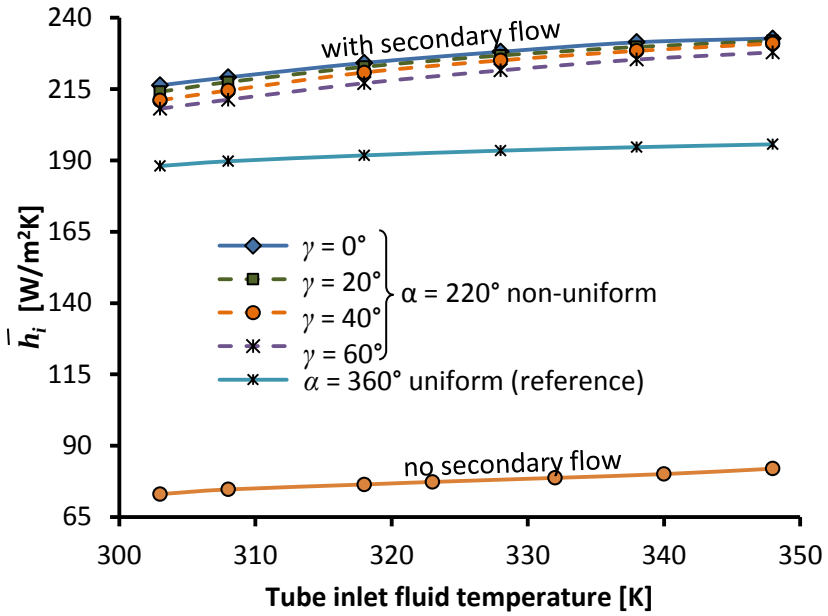

Figure 19 Average internal heat transfer coefficients for different fluid inlet temperatures and values of γ compared to the associated uniform heat flux distribution

Figure 19 shows the variations of average internal heat transfer coefficient for different inlet fluid temperature for α = 320° and γ = 0°, 20°, 30° and 40°, for an inlet Reynolds number of 800. For comparison purposes the associated reference fully uniform heat flux case is also included. Thus, all cases in this figure have the same incident heat transfer rate [W]. It was found that while maintaining the same ambient temperature, the average internal heat transfer coefficient increased with an increase in the inlet fluid temperature. This indicates the influence of pre-heating the inlet heat transfer fluid on the internal heat transfer coefficient of a circular tube. For the inlet fluid temperature range of 290 K to 360 K, the average internal heat transfer coefficient increased by 7% for γ = 0° and 9% for γ = 40°. The average internal heat transfer coefficients for the symmetrical cases are 1% to 5% higher than that of the asymmetrical cases for γ = 20° to 40° at the inlet fluid temperature of 308 K. Figure 19 also indicates the difference in the average internal heat transfer coefficients when the fluid

density is constant (no buoyancy-driven flow) and when the fluid density is temperature dependent (buoyancy-driven flow present) for the inlet temperature range of 290 K to 360 K. The average internal heat transfer coefficients for the uniform and non-uniform heat flux distributions increased up to 155% and 170% respectively higher than when the fluid density is constant. This indicates a very high significant internal heat transfer enhancement due to buoyancy-driven secondary flow effect.

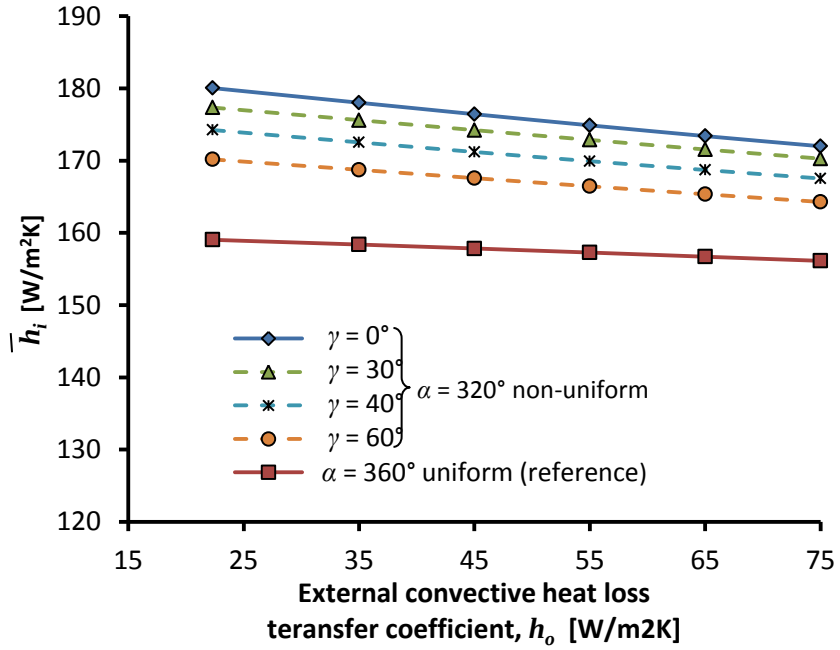

Figure 20 Influence of the external convective heat transfer coefficient on the average internal heat transfer coefficient for different values of γ at α = 320°

Figure 20 shows the influence of the external loss convective heat transfer coefficient, h_o, on the average internal heat transfer coefficient, for α = 320° with γ = 0°, 20°, 30° and 40°. The average internal heat transfer coefficient is coupled to the external heat transfer coefficient due to the impact that the tube wall temperature has on the secondary flow patterns. It was found that an increase in the external convective heat transfer coefficient (for an air velocity range of 4.36 m/s to 18.24 m/s), there was a decrease in the inner heat transfer coefficient. As before, the internal heat transfer also decreased with an increase in γ, due to the relative

sizes of fluid circulation vortexes. In Figure 21 the influence of the external convective heat transfer coefficient on the average internal heat transfer coefficient is shown, for γ = 20° with α = 160°, 220°, and 320°. Similar decreasing behaviour was observed for all angle span cases. The Ri number was found to be lower when Nu number was lower due to the impact the tube-wall heat flux distributions boundary has on the buoyancy-driven flow component within the tube. The external convective heat loss transfer coefficient increases with an increase in the air velocity around the tube outer surface. This results in an increase in an external convective heat loss and a decrease in the heat transfer rate from the external tube-wall surface to the heat transfer fluid in the tube.

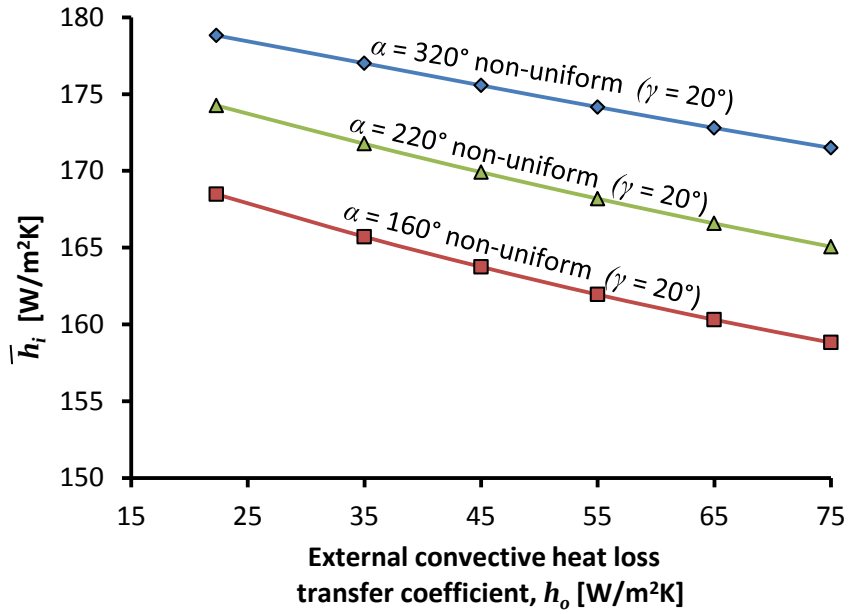

Figure 21 Influence of the external convective heat transfer coefficient on the average internal heat transfer coefficient for different values of α at γ = 20°

Friction Factors

Figure 22 presents the friction factors for different circumferential spans of the heat flux distribution cases shown in Figure 17 at different inlet Reynolds numbers. It gives a comparison of the friction factors for symmetrical (γ = 0°) and asymmetrical (γ = 30°) cases.

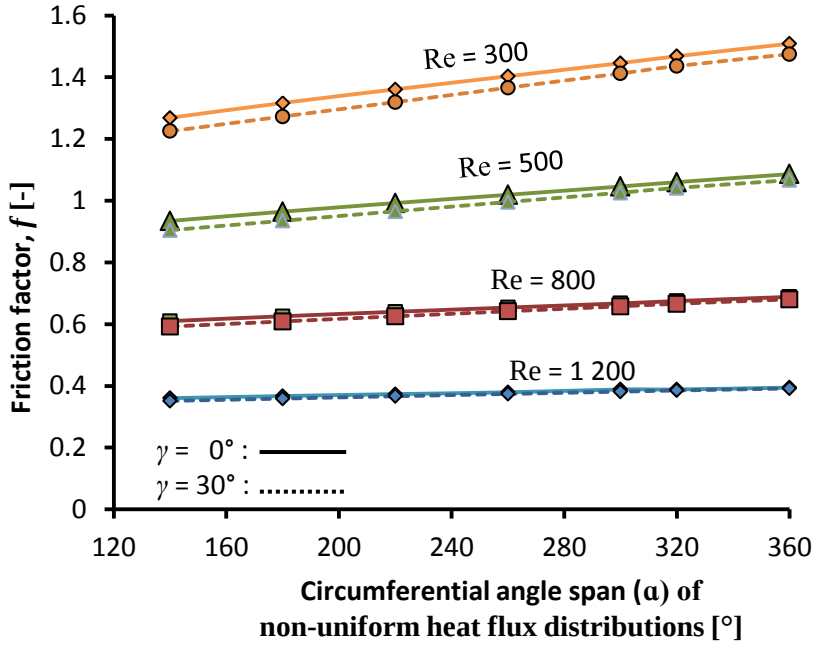

Figure 22 Friction factors at different angle spans for symmetrical and asymmetrical heat fluxes

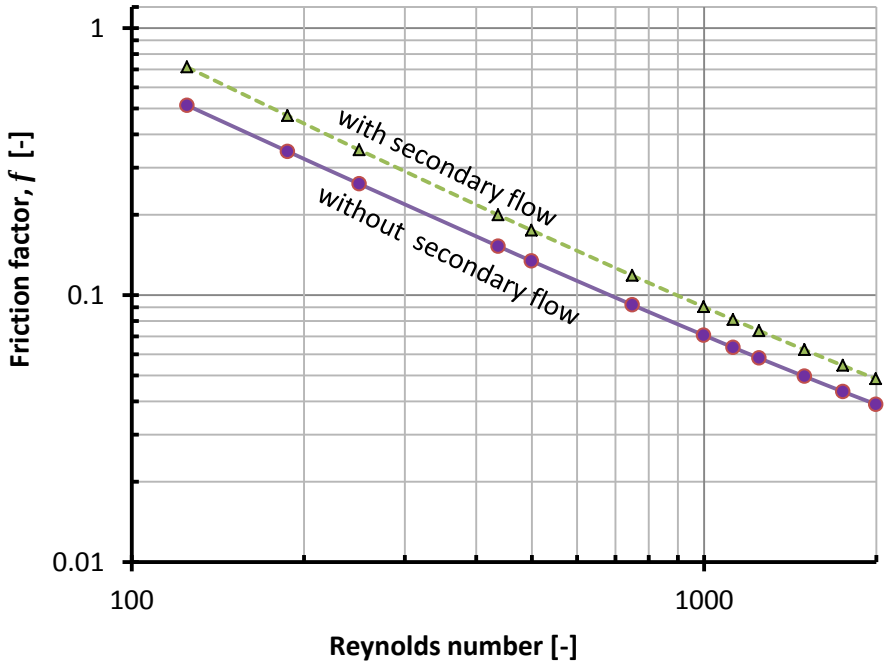

Figure 23 Friction factors for α = 320°and γ = 30° obtained with and without buoyancy-driven secondary flow for different inlet Reynolds numbers

As it should be expected, the friction factors decrease with Reynolds number. The friction factors for both symmetrical and asymmetrical cases were nearly constant through-out the angle span range, especially at higher Reynolds numbers, indicating that friction factor was only slightly influenced by an increase in the circumferential span of the heat flux distribution boundaries. Similar as with the heat transfer coefficients, the friction factor for the symmetrical heated case was only about 4% higher than for the 30° asymmetrical case at lower angle span for Re = 300. The importance of considering secondary flow is once again highlighted in Figure 23 which gives friction factors obtained with and without buoyancy-driven flow. It indicates that with or without buoyancy effects present, friction factors decreased with an increase in Reynolds number. When buoyancy-driven secondary flow was considered, the friction factor was higher by between 39% and 25% for α = 320° and γ = 30°, for the Reynolds number range of 130 to 2000, than when it was neglected.

Figure 24 shows the influence of the external convective heat transfer coefficient on the friction factor for the non-uniform heat flux distribution cases in Figure 18 for α = 320° and Re = 750. Also included are the associated fully uniform heat flux results for the same incident heat transfer rate [W]. It was found that the friction factor for both the symmetrical and asymmetrical cases decreased with an increase in the external loss convective heat transfer coefficient. It was also found that the friction factor decreased as the non-uniform heat flux distribution symmetry plane misaligned with the gravity field. This is due to the impact of conjugate heat transfer in the tube-wall on the secondary flow patterns within the tube. The fully uniform heat flux case had a significantly lower friction factor, indicating that the concentrated non-uniform heat flux profile on the outer tube surface from below had a significant role on the effective pressure drop.

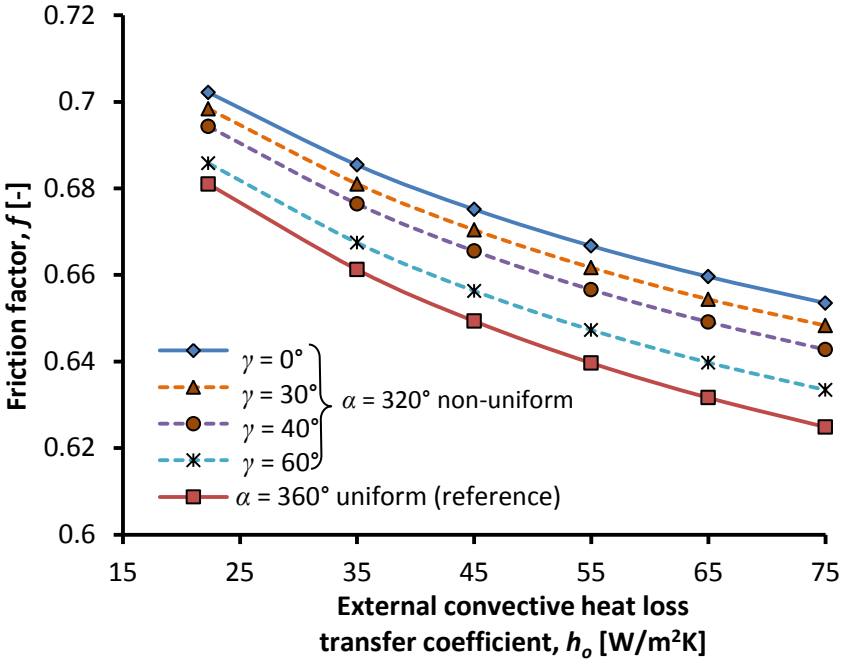

Figure 24 Influence of the external convective heat transfer coefficient on the friction factor for different values of γ at α = 320° and Re = 800

CONCLUSION

Internal heat transfer coefficients and friction factors for a horizontal circular tube were determined numerically for a laminar flow mixed convection heat transfer for different circumferential spans of a sinusoidal type symmetrical and asymmetrical non-uniform heat flux cases in terms of the gravitational field. The tube model under consideration could be employed for water heating as in the case of a solar thermal collector system. Three-dimensional steady-state with uniform inlet velocity was considered for inlet Reynolds numbers ranging from 130 to 2000. In addition to this, external wall heat loss was also considered via convection and radiation. The results indicate that the average internal heat transfer coefficient and friction factor decreased as the non-uniform heat flux distribution boundary misaligned with the symmetrical axis of the tube in terms of the gravitational direction. It was also found that the internal heat transfer coefficient increase with an increase

in the circumferential span of the symmetrical and asymmetrical non-uniform heat flux distribution boundaries, due to buoyancy effects. However, for cases having the same incident heat transfer rate, the non-uniform concentrated heat flux distributions had a much higher significant impact when compared to a fully uniform external heat flux boundary. In such cases the average heat transfer coefficients were higher than for the fully uniform heat flux cases for the conditions considered in this study. These differences are attributed to the buoyancy-induced secondary flow and non-uniformity in the tube wall temperature, indicating that appropriate heat flux distributions boundary must be considered, otherwise the internal heat transfer coefficient could be underestimated if uniform heat flux is considered where the actual heat flux distributions is non-uniform. Higher fluid inlet temperatures resulted in higher inner heat transfer coefficients, while increased outer tube wall heat flux losses resulted in lower inner heat transfer coefficients and friction factors.

Further study

The investigation of the influence of the asymmetrical non-uniform heat flux distribution boundary conditions needs to be extended for the case of a weak turbulent flow convective heat transfer in horizontal circular tubes applicable for water heating in solar thermal collector systems. Also, the use of ray-tracing software to improve the representation of the incident heat flux for specific application should be considered.

ACKNOWLEDGEMENTS

The funding obtained from the NRF, TESP, Stellenbosch University, University of Pretoria, SANERI/SANEDI, CSIR, EEDSM Hub and NAC is acknowledged and duly appreciated.

NOMENCLATURE

A	surface or cross sectional area, m^2
c_p	specific heat of the fluid, J/kg K
D	Diameter, m
f	Darcy friction factor
g	acceleration due to gravity, m/s^2
Gr	Grashof number
HCT	Heat collector element
$h, \overline{h}$	heat transfer coefficient and average heat transfer coefficient, W/m^2K
I	number of heated divisions
i	heated division number
k	thermal conductivity, W/m K
L, L_{TOT}	axial dimension and total axial length of tube, m
M	total number of the axial divisions
$\dot{m}$	mass flow rate, kg/s
(m, n)	numerical surface location
N	total number of the circumferential divisions
Nu, $\overline{\mathrm{Nu}}$	Nusselt number and average Nusselt number
P	pressure, Pa
Pr	Prandtl number
q	heat transfer rate, W
q''	heat flux, W/m^2
R	radius and average radius, m
r	radial coordinate, m
Re	Reynolds number

Ri	Richardson number
$T,\ \bar{T}$	temperature and average temperature, K
t	tube wall thickness, m
U	overall heat transfer coefficient, $W/m^2 K$
V	kinematic viscosity, m^2/s
$v,\ \bar{v}$	velocity and average velocity, m/s
x	axial coordinate, m

Greek Letters

α	angle span of the heated segment of the tube,°
β	thermal expansion coefficient of the heat transfer fluid, K^{-1}
γ	gravity inclination in terms of the heat flux symmetry plane,°
ε_{tu}	emissivity of the tube-wall surface
μ	viscosity, kg/ms
ρ	density of the heat transfer fluid, kg/m^3
σ_{SB}	Stefan-Boltzmann constant, $W/(m^2K^4)$
ϕ	angle span of each circumferential division, °, or tangential dimension

Subscripts

a	free stream air
atm	atmospheric
∞	radiant surroundings
b	bulk fluid property
$conv$	convection
f	fluid

g	glass
i	inner surface
m	at position m
n	at position n
o	outer surface
r	in radial direction
rad	radiation
tu	tube
w	wall
x	in axial direction
ϕ	in tangential direction

REFERENCES

[1] Arasu, A. V. and Sornakumar, T., Design, Manufacture and Testing of Fiberglass Reinforced Parabola Trough for Parabolic Trough Solar Collectors, Solar Energy, vol.81, pp. 1273–1279, 2007.

[2] Kalogirou, S. A., Solar Thermal Collectors and Applications, Progress in Energy and Combustion Science, vol. 30, pp. 231–295, 2004.

[3] Kalogirou, S. A. and Lloyd, S., Use of Solar Parabolic Trough Collectors for Hot Water Production in Cyprus. A Feasibility Study, Renewable Energy vol. 2, no. 2, pp. 117 -124, 1992.

[4] Vyas, M., Shailendra, S. S., Surendra, S., Dua, S. S. and Pranay, S. P., Thermal Performance Analysis of Water Heating System for a Parabolic Solar Concentrator: An Experimental Model Based Design, International Journal of Current Engineering and Technology, vol.4, no.5, pp. 3649- 3654, 2014.

[5] Eck, M., Uhlig, R., Mertins, M., Häberle, A. and Lerchenmüller, H., Thermal Load of Direct Steam-Generating Absorber Tubes with Large Diameter in Horizontal Linear Fresnel Collectors, Heat Transfer Engineering, vol. 28, no. 1, pp. 42-48, 2007.

[6] Okafor, I. F., Dirker, J. and Meyer, J. P., Influence of Circumferential Solar Heat Flux Distribution on the Heat Transfer Coefficients of Linear Fresnel Collector Absorber Tubes, Sol. Energy, vol. 107, pp. 381-397, 2014.

[7] Newell, J. P. H. and Bergles, A. E., Analysis of Combined Free and Forced Convection for Fully Developed Laminar Flow in Horizontal Tubes, J. of Heat Transfer, vol. 92, no. 1 pp. 83-93, 1970.

[8] Fand, R. M. and Keswani, K. K., Combined Transfer Natural and Forced Convection Heat from Horizontal Cylinders to Water, Intr. J. Heat Mass transfer, vol. 16, pp. 1175-1191, 1973.

[9] Mohammed, H. A. and Salman, Y. K., The Effects of Different Entrance Sections Lengths and Heating on Free and Forced Convective Heat Transfer Inside a Horizontal Circular Tube, International Communications in Heat and Mass Transfer, vol. 34, pp. 769–784, 2007.

[10] Chae, M.-S. and Chung, B.-J., Laminar Mixed-convection Experiments in Horizontal Pipes and Derivation of a Semi-empirical Buoyancy Coefficient, International Journal of Thermal Sciences, vol. 84, pp. 335-346, 2014.

[11] Lagana, A., Mixed Convection Heat Transfer in Vertical, Horizontal, and Inclined Pipes, M. Eng. Thesis, Dept. of Mechanical Engineering, McGill University Montreal, Canada, National Library of Canada, Acquisitions and Bibliographic Services, 1995.

[12] Mohammed, H. A. and Salman, Y. K., Experimental Investigation of Mixed Convection Heat Transfer for Thermally Developing Flow in a Horizontal Circular Cylinder, Applied Thermal Engineering vol. 27, pp. 1522–1533, 2007.

[13] Piva, S., Barozzi, G. S., and Collins, M. W., Combined Convection and Wall Conduction Effects in Laminar Pipe Flow: Numerical Predictions and Experimental Validation under Uniform Wall Heating, Heat and Mass Transfer, vol. 30, pp. 401-409, 1995.

[14] Boufendi, T. and Afrid, M., The Physical Aspect of Three-Dimensional Mixed Convection in a Uniformly Heated Horizontal Pipe, Sciences and Technologies, vol. 22, pp. 39-52, 2004.

[15] Boufendi, T. and Afrid, M., Three-Dimensional Conjugate Conduction-Mixed Convection with Variable Fluid Properties in a Heated Horizontal Pipe, Rev. Energ. Ren. vol. 8, pp. 1-18, 2005.

[16] Shome, B., Effect of Uncertainties in Fluid Properties on Mixed Convection Laminar Flow and Heat Transfer in a Uniformly Heated Smooth Tube', Numerical Heat Transfer, Part A, vol. 35, pp. 875-889, 1999.

[17] Prayagi, S. V. and Thombre, S. B., Parametric Studies on Buoyancy Induced Flow through Circular Pipes in Solar water heating system, International Journal of Engineering Science and Technology (IJEST) vol. 3, no. 1, pp. 616-627, 2011.

[18] Laouadi, A., Galanis, N., and Nguyen, C.T., Laminar Fully Developed Mixed Convection in Inclined Tubes Uniformly Heated on their Outer Surface, Numerical Heat Transfer, Part A, vol. 26, pp. 719-738. 1994.

[19] Bemier, M. A. and Baliga, B. R., Conjugate Conduction and Laminar Mixed Convection in Vertical Pipes for Upward Flow and Uniform Wall Heat Flux, Numerical Heat Transfer. Part A, vol. 21, pp. 313-332, 1992.

[20] Sadik, K., Shah, R. K., and Aung, W., Handbook of Single-Phase Convective Heat Transfer, A Wiley-Inter-Science Publication John Wiley & Sons New York, 1987.

[21] Ganesan, R., Narayanaswamy, R. and Perumal, K., Mixed Convection and Radiation Heat Transfer in a Horizontal Duct with Variable Wall Temperature, Heat Transfer Engineering, vol. 36 no. 4, pp. 335-345, 2015.

[22] Ashjaee, M., Yazdani, S., Bigham, S. and Yousefi, T., Experimental and Numerical Investigation on Free Convection From a Horizontal Cylinder Located Above an Adiabatic Surface, Heat Transfer Engineering, vol. 33 no. 3, pp. 213-224, 2012.

[23] Karimi, F., Xu, H., Zhiyun Wang, Z., Yang, M. and Zhang, Y., Numerical Simulation of Steady Mixed Convection around Two Heated Circular Cylinders in a Square Enclosure, Heat Transfer Engineering, vol. 37(1), pp. 64–75, 2016.

[24] Yapici, K. and Salih Obut, S., Laminar Mixed-Convection Heat Transfer in a Lid-Driven Cavity with Modified Heated Wall, Heat Transfer Engineering, vol. 36(3), pp. 303 –314, 2015.

[25] Zeitoun, O., Heat Transfer for Laminar Flow in Partially Heated Tubes, Alexandria Engineering Journal, Alexandria University, Egypt, vol. 41, no. 2, pp. 205-212, 2002.

[26] Zeitoun, O., Conjugate Laminar Forced Convection in Partially Heated Tubes ACOMEN: Second International Conference on Advanced Computational Methods In Engineering, Belgium, pp. 1-25, 2002.

[27] Patankar, S.V., Numerical Heat Transfer and Fluid Flow, Hemisphere Publishing Corporation, United States of America, 1980.

[28] Stynes, J. K. and Ihas, B., Absorber Alignment Measurement Tool for Solar Parabolic Trough Collectors , ASME 6th International Conference on Energy Sustainability & 10th Fuel Cell Science, Engineering and Technology Conference, San Diego, California, July 23–26, 2012.

[29] Stynes, J. K. and Ihas, B., Slope Error Measurement Tool for Solar Parabolic Trough Collectors, World Renewable Energy Forum Denver, Colorado, May 13–17, 2012

[30] Christian, J. M. and Ho, C. K., Finite Element Modeling and Ray Tracing of Parabolic Trough Collector for Evaluation of Optical Intercept Factor with Gravity Loading, Proceedings of the ASME 5th International Conference on Energy Sustainability, 2011.

[31] Bazdidi-Tehrani, F., Aghaamini, M. and Moghaddam, S., Radiation Effects on Turbulent Mixed Convection in an Asymmetrically Heated Vertical Channel, Heat Transfer Engineering, vol. 35 no. 5, pp. 475-497, 2017.

[32] Satyamurty, V. V. and Repaka, R., Superposition Relations for Forced Convective Local Nusselt Numbers for Flow through Asymmetrically Heated Parallel-Plate Channels, Heat Transfer Engineering, vol. 32(6), pp. 476–484, 2011.

[33] Kim, W. T. and Boehm, R. F., Laminar Buoyancy-Enhanced Convection Flows on Repeated Blocks with Asymmetric Heating, Numerical Heat Transfer, Part A: Applications International Journal of Computation and Methodology vo. 22 (4), pp. 421-434, 2010.

[34] Habchi S. and Acharya S., Laminar Mixed Convection in a Symmetrically or Asymmetrically Heated Vertical Channel, Journal Numerical Heat Transfer vol. 9 (5), pp. 605-618, 2007.

[35] Osborne, D. G. and Incropera, F. P., Laminar Mixed Convection Heat Transfer for Flow between Horizontal Parallel Plates with Asymmetric Heating, International Journal of Heat and Mass Transfer, vol. 28, no. 1, pp. 207-217, 1985.

[36] Wirz, M., Roesle M. and Steinfeld A., Three-Dimensional Optical and Thermal Numerical Model of Solar Tubular Receivers in Parabolic Trough Concentrators, Journal of Solar Energy Engineering, 134, 2012

[37] Cengel, Y. A., Heat and Mass Transfer: A Practical Approach, Third Edition Published by McGraw-Hill Companies, Inc. 1221 Avenue of the Americas, New York, NY 10020, 2007.

[38] Rajput, R. K., Heat and Mass Transfer in SI Units, Second Edition, Published by S. Chand and Company Ltd, Ram Nagar, New Delhi - 110 055, 2005.

[39] Tiwari, G. N., Solar Energy Fundamental, Design, Modelling and Applications, Narosa Publishing House, 22 Daryaganj, Delhi, India, 2006.

[40] Hameury, J., Hay, B., and Filtz J-R., Measurement of Total Hemispherical Emissivity

Using a Calorimetric Technique, Laboratoire National de Métrologie d'Essais (LNE), 29 Avenue Roger Hennequin, 78197 TRAPPES Cedex, France , pp.1-14, 2005.

[41] ANSYS Fluent version 14.0, Users' Guide ANSYS, Release 14.0 Incorporated, Southpointe 275 Technology Drive Canonsburg, PA 15317, 2011.

[42] Popiel C. O. and Wojtkowiak J., Simple Formulas for Thermophysical Properties of Liquid Water for Heat Transfer Calculations (from 0°C to 150°C), Heat Transfer Engineering, vol. 19, no. 3 pp. 87-101, 1998.

[43] Ferziger, J. H. and Perifi, M., Computational Methods for Fluid Dynamics, 3 Rev. Ed.- Berlin; Heidelberg; Hong Kong; London; Milan; Paris; Tokyo: Springer, 2002.

[44] Hallquist, M., Heat Transfer and Pressure Drop Characteristics of Smooth Tubes at A Constant Heat Flux in the Transitional Flow Regime, M. Eng. Thesis, Dept. of Mechanical and Aeronautical Engineering, University of Pretoria, South Africa, 2011.

[45] Wen, D. and Ding, Y., Experimental Investigation into Convective Heat Transfer of Nanofluids at the Entrance Region under Laminar Flow Conditions, International Journal of Heat and Mass Transfer, vol. 47, pp. 5181- 5188, 2004.

[46] Ghajar, A. J. and Tam, L.-M., Flow Regime Map for a Horizontal Pipe with Uniform Wall Heat Flux and Three Inlet Configurations, Experimental Thermal and Fluid Science, vol.10, pp. 287-297, 1995.

[47] Moss, T. A. and Brosseau, D. A., Final Test Results for the Schott HCE on a LS-2 Collector, Solar Technologies, Sandia National Laboratories Albuquerque, New Mexico 87185 and Livermore, California 94550, NM 87185-1127, 2005.

[48] Properties of Syltherm® 800 Heat Transfer Liquid, Midland, MI: Dow Corning Corporation, 1985.

[49] Forristall, R., Heat Transfer Analysis and Modeling of a Parabolic Trough Solar Receiver Implemented in Engineering Equation Solver National Renewable Energy Laboratory 1617 Cole Boulevard Golden, Colorado 80401-3393, 2003.

BIOGRAPHICAL INFORMATION OF THE AUTHORS

Izuchukwu F. Okafor is a PhD student in the Clean Energy Research Group in the Department of Mechanical and Aeronautical Engineering at the University of Pretoria, South Africa. His research interests are in heat transfers in renewable energy systems and currently working on the circumferential non-uniform heat flux distributions boundary conditions for improving the thermal performance modelling of horizontal circular tubes for single-phase water heating in solar thermal collector applications.

Jaco Dirker is an Associate Professor in the Department of Mechanical and Aeronautical Engineering at the University of Pretoria, South Africa. He obtained his Ph.D. in mechanical engineering from the Rand Afrikaans University in Johannesburg, South Africa. His research interests include convective heat transfer in macro- and microchannels, and thermal system optimization.

Josua P. Meyer is a Professor and Chair of the School of Engineering and also head of the Department of Mechanical and Aeronautical Engineering at the University of Pretoria, South Africa. He specializes in heat transfer, fluid mechanics, and thermodynamic aspects of heating, ventilation, and air conditioning. He is the author and co-author of more than 400 articles, conference papers, and patents, and has received various prestigious awards for his research. He is also a fellow or member of various professional institutes and societies and is regularly invited as a keynote speaker at local and international conferences. He has received various teaching awards as Lecturer of the Year and he has received three awards from the University of Pretoria as an exceptional achiever. In 2011, he was evaluated by the National Research Foundation (NRF) as an established researcher who enjoys considerable international recognition for the high quality and impact of his recent research outputs. He is an associate editor of both Heat Transfer Engineering and Journal of Porous Media.